

**MASARYKOVA UNIVERZITA**  
Přírodovědecká fakulta  
Ústav teoretické fyziky a astrofyziky

**BAKALÁŘSKÁ PRÁCE**

**Brno 2020**

**Michaela Vítková**

**M A S A R Y K O V A  
U N I V E R Z I T A**

Přírodovědecká fakulta  
Ústav teoretické fyziky a astrofyziky

---

**Vliv kadence a rozptylu dat na  
přesnost určení parametrů  
exoplanetárních tranzitů**

Bakalářská práce

**Michaela Vítková**

Vedoucí bakalářské práce:  
Mgr. Marek Skarka, Ph.D.

Brno 2020

## Bibliografický záznam

**Autor:** Michaela Vítková  
Přírodovědecká fakulta, Masarykova univerzita  
Ústav teoretické fyziky a astrofyziky

**Název práce:** Vliv kadence a rozptylu dat na přesnost určení parametrů exoplanetárních tranzitů

**Studijní program:** Fyzika

**Směr:** Fyzika

**Vedoucí práce:** Mgr. Marek Skarka, Ph.D.

**Konzultant:** Mgr. Martin Blažek

**Akademický rok:** 2019/2020

**Počet stran:** viii + 37

**Klíčová slova:** extrasolární planeta, exoplanetární tranzit, světelná křivka, kadence dat

## Bibliographic record

**Author:** Michaela Vítková  
Faculty of Science, Masaryk University  
Department of Theoretical Physics and  
Astrophysics

**Title of Thesis:** Impact of data sampling and quality  
on the precision of exoplanetary transit  
parameters

**Degree Programme:** Physics

**Field of study:** Physics

**Supervisor:** Mgr. Marek Skarka, PhD

**Advisor:** Mgr. Martin Blažek

**Academic Year:** 2019/2020

**Number of Pages:** viii + 37

**Keywords:** extrasolar planet, exoplanetary transit,  
light curve, cadence of data

## Abstrakt

V této bakalářské práci se zabýváme vlivem kadence a rozptylu dat na přesnost určení parametrů exoplanetárních tranzitů. Z exoplanetárního tranzitu lze určit řada vlastností pozorované soustavy jako například poměr poloměru planety ku poloměru hvězdy  $R_p/R_s$ , inklinaci  $i$ , hlavní poloosu dráhy  $a$  a čas středu tranzitu  $t_0$ . Pro určování těchto parametrů jsme nasimulovali a zpětně analyzovali světelné křivky fiktivní exoplanety typu tzv. horkého Jupitera obíhající hvězdu slunečního typu. Simulaci a analýzu jsme prováděli pomocí Python balíku `PyLightcurve`. Pro lepší přiblížení reálným pozorováním jsme při generování křivek brali v úvahu kadenci a rozptyl dat základních vesmírných misí Kepler, TESS a PLATO a pozemních misí jako SuperWASP. Z výsledků můžeme říct, že určení exoplanetárních parametrů z dat 30 minutové kadence a šumu 10000 ppm může být velmi zavádějící a není pro bližší charakterizaci exoplanet vyhovující, například při určování poloměru exoplanety z těchto dat byla chyba určení 19.5 %. Při nejmenším rozptylu dat (200 ppm) byla chyba určení poloměru exoplanety pouze 0.5 %. Dle očekávání jsme pro tento rozptyl dat dostali nejlepší výsledky pro všechny parametry a můžeme říct, že při nízkém šumu nezáleží na použité kadenci.

## Abstract

In this bachelor thesis we deal with the impact of data sampling and quality on the precision of exoplanetary transit parameters. From the exoplanetary transit, a number of properties of the observed system can be determined, such as the ratio of the planet's radius to the star's radius  $R_p/R_s$ , the inclination  $i$ , the semi-major axis  $a$ , and the time of the center of the transit  $t_0$ . To determine these parameters, we simulated and retrospectively analyzed the light curves of the fictive exoplanet the so-called hot Jupiter orbiting a solar-type star. Simulations and analysis was performed using the python package `PyLightcurve`. For a better approximation of real observations, we took into account the cadence of data and data noise of the main space missions Kepler, TESS and PLATO and ground missions such as SuperWASP when generating the light curves. From the results we can say that the determination of parameters from the data of 30 minutes cadence and noise 10000 ppm can be very misleading and is not suitable for further characterization of exoplanets, for example when determining the radius of the exoplanet from these data the relative standart deviation was 19.5%. For the smallest scatter (200 ppm) was relative standart deviation only 0.5%. As expected, we got the best results for this data scatter for all parameters and we can say that cadence has almost no impact on the results.

ZADÁNÍ  
BAKALÁŘSKÉ PRÁCE

Akademický rok: 2019/2020

---

|                   |                                       |
|-------------------|---------------------------------------|
| <b>Ústav:</b>     | Ústav teoretické fyziky a astrofyziky |
| <b>Studentka:</b> | Michaela Vítková                      |
| <b>Program:</b>   | Fyzika                                |
| <b>Obor:</b>      | Fyzika                                |

---

Ředitel *Ústavu teoretické fyziky a astrofyziky* PřF MU Vám ve smyslu Studijního a zkušebního řádu MU určuje bakalářskou práci s názvem:

---

|                               |   |
|-------------------------------|---|
| <b>Název práce:</b>           | Vliv kadence a rozptylu dat na přesnost určení parametrů exoplanetárních tranzitů       |
| <b>Název práce anglicky:</b>  | Impact of data sampling and quality on the precision of exoplanetary transit parameters |
| <b>Jazyk závěrečné práce:</b> | angličtina  |

---

**Oficiální zadání:**

Jednou ze základních metod pro výzkum a objevování exoplanet je metoda tranzitu. V dnešní době jsou k dispozici data z malých dalekohledů na zemském povrchu, ale také data pořízená z vesmíru. Existuje tedy celá řada různě kvalitních datových sad pořízených různými přístroji. Cílem práce je odhadnout jaký vliv na přesnost určení parametrů tranzitu, zejména jeho hloubky, má kadence a rozptyl použitých dat.

**Literatura:**

PERRYMAN, M. A. C. *The exoplanet handbook*. Second edition. Cambridge: Cambridge University Press, 2018. xx, 952. ISBN 9781108419772.

MIKULÁŠEK, Zdeněk a Miloslav ZEJDA. *Úvod do studia proměnných hvězd*. Nové rozšířené vydání. Brno: MU, 2013.

---

|                            |                          |
|----------------------------|--------------------------|
| <b>Vedoucí práce:</b>      | Mgr. Marek Skarka, Ph.D. |
| <b>Konzultant:</b>         | Mgr. Martin Blažek       |
| <b>Datum zadání práce:</b> | 28. 11. 2019             |
| <b>V Brně dne:</b>         | 19. 12. 2019             |

---

Souhlasím se zadáním (podpis, datum):

.....  
Michaela Vítková  
studentka

.....  
Mgr. Marek Skarka, Ph.D.  
vedoucí práce

.....  
prof. Rikard von Unge, Ph.D.  
ředitel Ústavu teoretické fyziky a  
astrofyziky

## **Poděkování**

Na tomto místě bych chtěla poděkovat svému vedoucímu Mgr. Marku Skarkovi, Ph.D. za jeho neutuchající optimismus, podporu, trpělivost a odborné vedení této práce. Také bych chtěla poděkovat svým rodičům a bratrovi za veškerou podporu při studiu.

## **Prohlášení**

Prohlašuji, že jsem svoji bakalářskou práci vypracovala samostatně pod vedením vedoucího práce s využitím informačních zdrojů, které jsou v práci citovány.

Brno 17. srpna 2020

---

Podpis autora

# Contents

|          |   |           |
|----------|---|-----------|
| <b>1</b> | <b>Overview of the exoplanetary research</b>        | <b>1</b>  |
| 1.1      | Introduction . . . . .                              | 1         |
| 1.2      | History . . . . .                                   | 2         |
| 1.3      | Methods of exoplanetary research . . . . .          | 3         |
| 1.4      | Current research on transiting exoplanets . . . . . | 6         |
| 1.4.1    | Ground-based missions . . . . .                     | 7         |
| 1.4.2    | Space missions . . . . .                            | 7         |
| <b>2</b> | <b>Transit light curves</b>                         | <b>9</b>  |
| 2.1      | Geometry of transit . . . . .                       | 10        |
| 2.2      | Limb-darkening . . . . .                            | 12        |
| <b>3</b> | <b>Generating the light curves</b>                  | <b>15</b> |
| 3.1      | PyLightcurve . . . . .                              | 15        |
| <b>4</b> | <b>Analysis of light curves</b>                     | <b>20</b> |
| 4.1      | Light curves and fitting . . . . .                  | 20        |
| 4.2      | Results of analysis . . . . .                       | 20        |
| 4.2.1    | Planet radius $R_p$ . . . . .                       | 22        |
| 4.2.2    | Semi-major axis $a$ . . . . .                       | 24        |
| 4.2.3    | Inclination $i$ . . . . .                           | 27        |
| 4.2.4    | Transit mid-time $t_0$ . . . . .                    | 29        |
| <b>5</b> | <b>Discussion and conclusions</b>                   | <b>31</b> |
|          | <b>Bibliography</b>                                 | <b>33</b> |

# Overview of the exoplanetary research

## 1.1 Introduction

Probably everyone has ever wondered if there is anyone else in the Universe or we are alone in this vast dark forest. If we consider it appropriate to look for other forms of life, the best way will be to study exoplanets. Extrasolar planets, or abbreviated exoplanets, are planets outside of our Solar system. Exoplanetary research has experienced huge progress in recent years. Until a few decades ago, it was unthinkable for some people that we could detect other worlds. Today we know about four thousand confirmed exoplanets and over five thousand candidates [E01]. These bodies, invisible to the naked eye, could even provide suitable conditions for the development of life. The huge contrast between the star and the orbiting planet is making it complicated to detect these objects. Nevertheless, we have several possibilities for detection and investigation of exoplanets.

In this work, we focus on the method of transit, where we can observe the planet passing directly between its star and an observer. Thus, we observe a decrease in the brightness of the star. It is possible to determine the size of the orbiting planet and other characteristics from the light curve. Therefore the measured data must be of the highest quality. In this thesis, we study the difference between the transit parameters determined from different data sets.

The work is divided into five chapters. In Chapter 1, we summarize the history, detection methods and current research on exoplanets. In Chapter 2, we describe properties of light curves. Description of how we proceeded in generating light curves using `PyLightcurve` code is in Chapter 3. The analysis of these curves is described in Chapter 4. In Chapter 5, we summarize the results.

## 1.2 History

Since ancient times, people have considered whether there are worlds outside the Solar system, but at that time, it was not possible to confirm these assumptions. In the 16th century, it was Giordano Bruno who spoke of an infinite universe full of sun-like stars, each surrounded by planets with intelligent life (Maor, 1987). In 1952, Otto Struve mentioned in his Proposal for a High-Precision Stellar Radial Velocity Work that there is no reason for the planets not to be closer to their parent star than in the Solar system (Struve, 1952).

The oldest record of a potential exoplanet was made in 1917 when Adrian van Maanen observed the subtle motion of Van Maanen 2 relative to other stars. Now we know that van Maanen's star is a white dwarf without an orbiting planet (van Maanen, 1917). The scientists also agreed that a single white dwarf with heavy elements in the spectrum could have a ring from the dust of the torn-apart planet (Graham et al., 1990).

The first confirmed detection of the exoplanet was in 1992 when three planets orbiting the pulsar PSR B1257+12 were discovered. These exoplanets are not only the first confirmed detections but are also the first detected pulsar planets (Wolszczan and Frail, 1992).

In 1995, the first detection of a planet orbiting a main sequence star was confirmed. For a G-type star called 51 Pegasi, there was a giant Jupiter-like planet detected using the radial velocity measurements (Mayor and Queloz, 1995). In 2017, water was discovered in the atmosphere of this exoplanet (Birkby et al., 2017). The Nobel Prize was awarded to Michel Mayor and Didier Queloz for the discovery of this exoplanet in 2019.

HD 209458b was detected in 1999. It is the first exoplanet that was observed using the transit method. It is also the first exoplanet to be detected by more than one method. First using radial velocities and via transit photometry (Castellano et al., 2000).

A planet fully comparable with the Earth was discovered in 2015. This planet is called Kepler-452b and orbits within the habitable zone of Sun-like star in constellation Cygnus (Jenkins et al., 2015).

In 2016, an Earth-mass planet was discovered in the habitable zone that orbits around Proxima Centauri, which is the nearest star to the Solar system (Anglada-Escudé et al., 2016).

In 2018, it has been observed that there could be also exoplanets in other galaxies than in the Milky Way Galaxy (Dai and Guerras, 2018; Bhatiani et al., 2019). The discoveries of the exoplanets are gradually increasing, as can be seen from the plot in Figure 1.1.

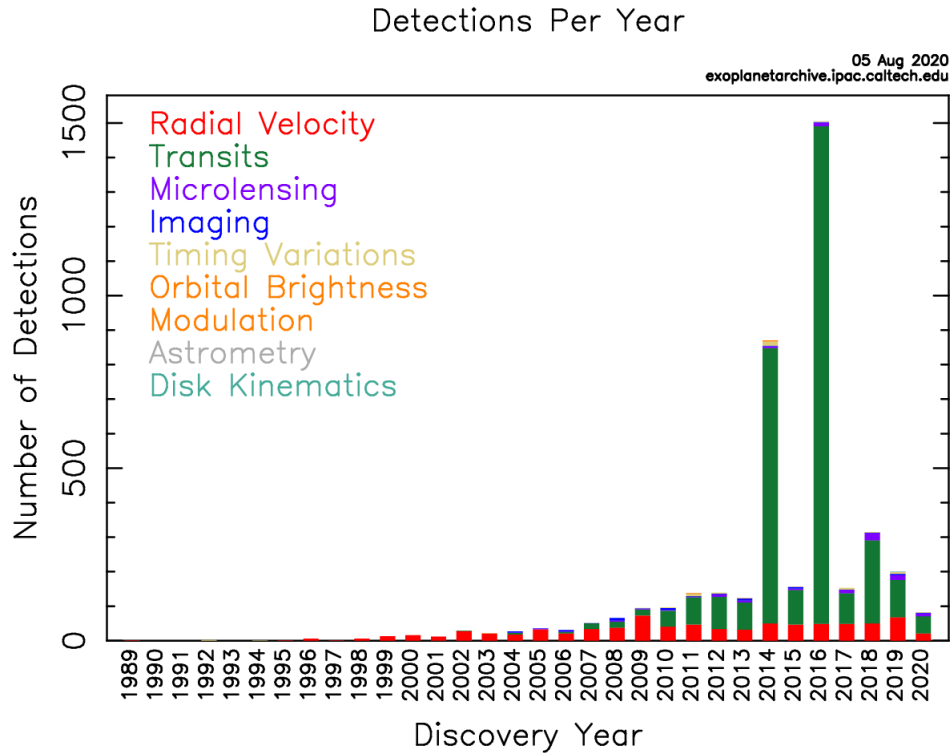


Figure 1.1: Number of detections per year [E02].

### 1.3 Methods of exoplanetary research

There are several ways to detect exoplanets. The main three are radial velocity, transit photometry and microlensing methods. There are other methods such as astrometry or direct imaging. The most successful is transit photometry with 3187 confirmed exoplanets, and the least successful is astrometry with only one confirmed exoplanet [E02].

#### Astrometry

Only one exoplanet was discovered by this method [E01]. Astrometry is using the same phenomena as radial velocity, which is that the star and the planet are orbiting around the same centre of gravity. Thus, the star is periodically moving on the star background. The principle of this method is shown in Figure 1.2. The main reason why only one exoplanet has been discovered so far is that this method requires very precise measurements of a star's position in the sky over a long time. Astrometry also requires best-quality optics, and because of Earth's atmosphere, it is difficult to perform it from the surface (Perryman, 2018).

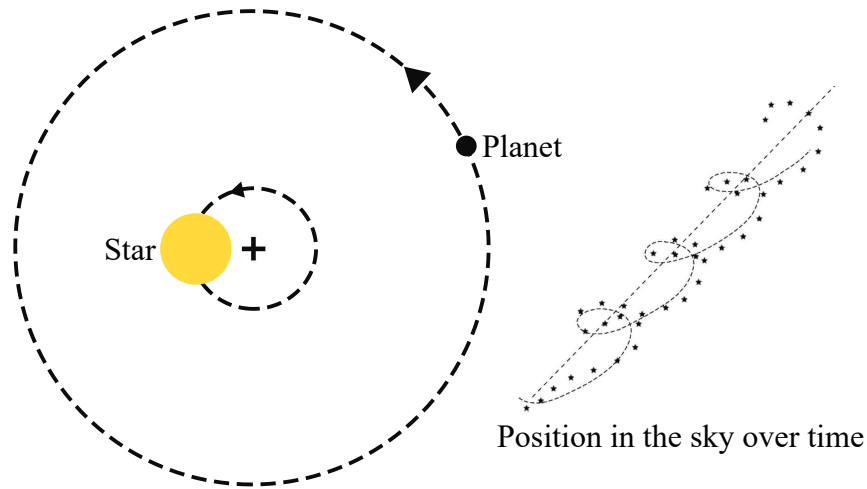


Figure 1.2: The principle of the astrometry method. In the figure on the right, the position in the sky over time is shown, the straight dashed line shows the motion of the barycenter of the observed system viewed from the solar system barycenter, the curved dashed line shows the effect of the orbital motion of the Earth around the Sun and the star-dotted line shows the motion of the star as a result of orbiting planet.

### Microensing

By this method, 96 exoplanets were discovered [E02]. Microensing is based on the gravitational lens effect. An object in the foreground represents the lens, and a source is an object in the background. When the lens and the source are almost exactly aligned, the lens bends the light of a faint background object. If the lens is a star with an orbiting planet, then the gravitational field of the planet can make a detectable contribution to the lensing effect. The principle of this method is shown in Figure 1.3. This method allows the detection of very distant exoplanets. The mass of the planet and its orbital radius can be estimated using this method (Perryman, 2018).

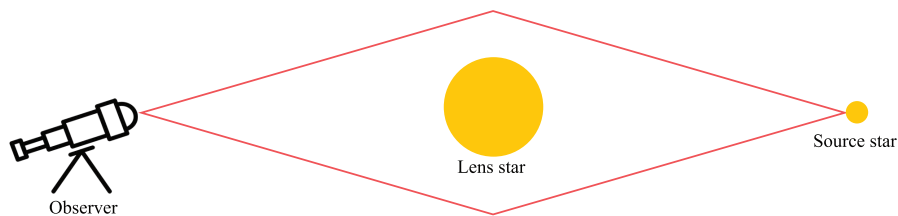


Figure 1.3: The principle of microensing method.

### Radial velocity

Radial velocity method is also known as Doppler spectroscopy. Via this method, 810 exoplanets were discovered [E02]. This method is based on the change of the spectrum of light emitted by the star. This change is caused by gravitational interaction between a star and a planet. They are orbiting around the same centre of gravity making the star moving closer and further from the observer. When the star is moving away from the observer wavelength increases and redshift can be observed. If the star is moving towards the observer blueshift can be detected. In Figure 1.4, the principle of this method is shown. When these shifts are observed regularly it is almost clear that they are caused by an unseen body. The minimum mass of the planet can be determined from the changes in the star's radial velocity (Perryman, 2018).

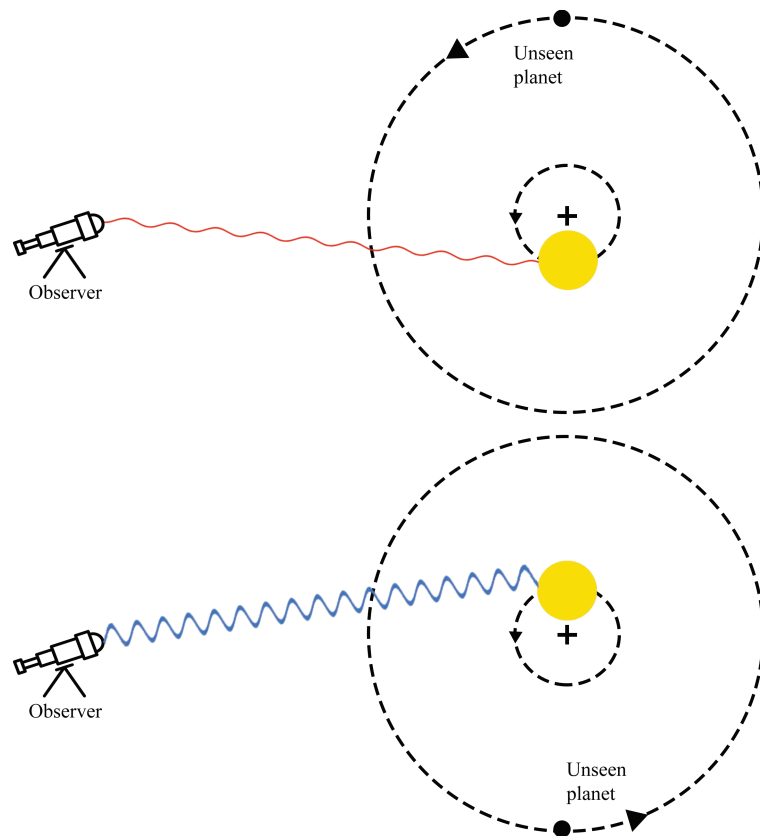


Figure 1.4: The principle of radial velocity method.

### Direct imaging

Using this method, 50 exoplanets were discovered [E02]. This method is using the reflected light from the parent star for imaging in the visible or thermal emission of the planet for imaging in the infrared. In the infrared, the planet is brighter than it is in visible. Coronagraphs in telescopes are used to block light from the parent star before it reaches the detector. When the light from the parent star is blocked it is easier to spot the orbiting planet. This method is suitable for planets that orbit at great distances from their stars and are particularly large (Perryman, 2018).

### Transit photometry

Transit photometry is the most successful method with 3187 confirmed exoplanets [E02]. This method is based on observations of the star's flux. When the planet passes directly between an observer and the parent star, luminosity decreases. Semi-major axis, planet radius, eccentricity, and inclination can be estimated from the observations. The main disadvantage of this method is that the transit is observable only when the orbit of the orbiting planet is perfectly aligned with the observer. Another disadvantage is that the luminosity decrease can be caused also by different phenomena. For example, starspot or it could be a multi-star system (Perryman, 2018). The principle of this method is shown in Figure 1.5. A more detailed description of this method is in section 2.1.

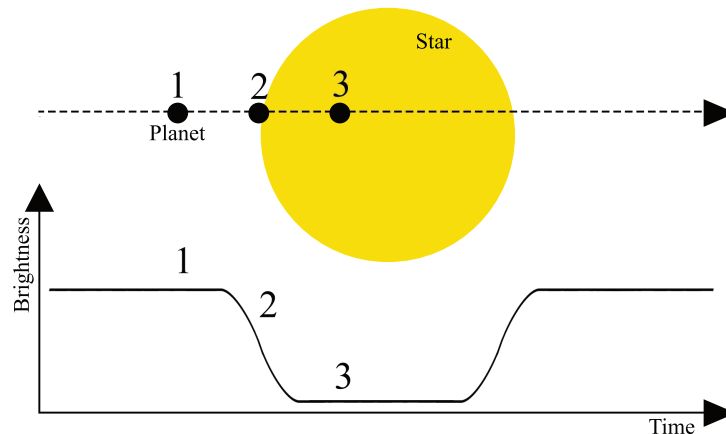


Figure 1.5: The principle of transit photometry.

## 1.4 Current research on transiting exoplanets

Since the detection of the transit highly depends on the system alignment, it is more efficient to do big sky surveys that scan large areas on the sky than the photometry of individual stars. In the following section, some of the ground-based and space missions are mentioned.

### 1.4.1 Ground-based missions

#### WASP

WASP stands for Wide Angle Search for Planets. It is the most successful ground-based project with more than 150 confirmed exoplanets [E03]. The first exoplanets were confirmed by this project in 2006 and are called WASP-1b and WASP-2b (Collier Cameron et al., 2007). WASP is an international collaboration of several organizations. It can scan the whole sky using two observatories. One is called SuperWASP-North and is located at Roque de los Muchachos Observatory at the Canary Islands. The other one is called WASP-South and is located at the South African Astronomical Observatory in South Africa. Each of these observatories uses eight wide-angle cameras monitoring stars with apparent visual magnitude from 7 to 15 mag (Pollacco et al., 2006).

#### KELT

KELT stands for The Kilodegree Extremely Little Telescope (Pepper et al., 2007). So far, 26 exoplanets have been discovered using KELT. KELT consists of two telescopes covering the north and south hemispheres. KELT-North is located at Winer Observatory in Arizona and started operations in 2006, KELT-South is located at South African Astronomical Observatory in South Africa and started operations in 2009 [E04]. Observed stars have apparent visual magnitude from 8 to 10 mag. One of the planets discovered by KELT is KELT-9b which is the hottest planet ever detected (Collins et al., 2016).

#### The HAT exoplanet surveys

The Hungarian Automated Telescope Network (HATNet) consists of seven small telescopes, five of them are located in Arizona, and the other two are in Hawaii (Bakos et al., 2004). Using this network, 63 exoplanets were discovered since 2003 [E05]. HATSouth survey is an extension for observations of the southern hemisphere which is operating since 2009 and discovered 71 exoplanets [E06]. It is a network of six astrograph telescope systems operating from South America, Africa, and Australia (Bakos et al., 2013). Another future expansion is HATPI and it will be able to monitor the entire sky visible from its site in Chile [E07].

### 1.4.2 Space missions

The study of exoplanets is difficult from the Earth's surface because it highly depends on observation conditions. This is why a large number of space missions for the detection of exoplanets have been and continue to be created.

#### CoRoT

CoRoT is an abbreviation for Convection, Rotation and planetary Transits. It was the first space mission designed for exoplanetary research. This space mission

was in operation from December 2006 to June 2014. Planned mission duration was 2.5 years, but it was extended and lasted for 7 years (Auvergne et al., 2009). During these seven years, 32 exoplanets were discovered [E08]. One of these planets is CoRoT-7b which is the first detected rocky planet (Léger et al., 2009; Rouan et al., 2010).

### **Kepler**

Kepler was a space mission launched by NASA named after Johannes Kepler. It was in operation since May 2009 and planned mission duration was 3.5 years. In July 2012, one of the spacecraft's four reaction wheels failed and in May 2013, the second reaction wheel failed which made it impossible to continue in mission because three wheels were necessary for the observations. In May 2014 it was announced that Kepler mission will be extended to the K2 mission. After nine years in October 2018 the spacecraft ran out of fuel and mission come to an end. After these 9 years, the total number of exoplanets discovered by Kepler is more than 2300, making it the most successful mission so far [E02]; [E09]; [E10]; (Koch et al., 2010; Van Cleve and Caldwell, 2016).

### **TESS**

The Transiting Exoplanet Survey Satellite is NASA's currently operating space telescope. TESS is a Kepler space telescope successor. It was launched in April 2018, and the planned mission duration is two years. The primary goal is to discover planets smaller than Neptune that transit stars bright enough that follow-up spectroscopic observations can be done (Ricker et al., 2015; Schliegel, 2017). TESS extended mission started in July 2020. The original full-frame image cadence (30 minutes) is changed to 10 minutes [E11]. Up to date, 66 exoplanets were confirmed and 2136 of candidates is waiting for confirmation [E02].

### **PLATO**

PLANetary Transits and Oscillations of stars is the European Space Agency space telescope to be launched in 2026. PLATO primary mission is to study terrestrial exoplanets orbiting Sun-like stars in the habitable zone. The planned duration of this mission is 4 years with the possibility to be extended for additional 4 years (Plato, 2017), [E12].

### **ARIEL**

The Atmospheric Remote-sensing Infrared Exoplanet Large-survey is the European Space Agency space telescope to be launched in 2028. The mission of this space telescope will be to observe known transiting exoplanets and to study and characterize exoplanet atmospheres via spectroscopy. The duration of this mission is planned for 4 years (Puig et al., 2016), [E13].

## Transit light curves

Transit can be observed only when the system of star and exoplanet is properly aligned, so that planet passes directly between an observer and the parent star. The condition for the realization of transit is as follows (Sackett, 1999):

$$a \cos i \leq R_p + R_s, \quad (2.1)$$

where  $a$  is the semi-major axis,  $i$  the inclination, which represents the angle of the orbit of the exoplanet with respect to the plane perpendicular to the plane of observation,  $R_p$  is the radius of the planet and  $R_s$  is the radius of the parent star. This condition is shown in Figure 2.1.

This almost perfect alignment plays a large role in observing transiting exoplanets. Another criterion for observation of the transit is the depth of the transit. For example planet with a radius similar to Jupiter radius orbiting a star with Solar radius results in 1% star flux drop.

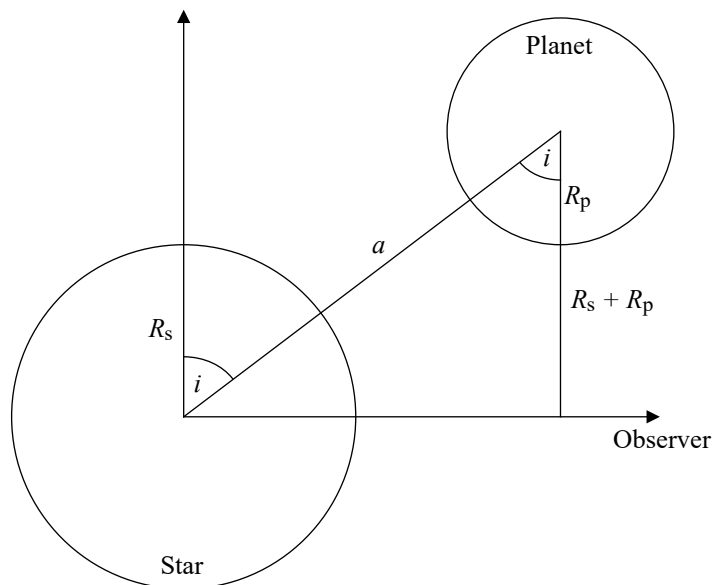


Figure 2.1: The geometry of the condition for transit realization.

The probability of transit for a randomly oriented planet on a circular orbit is given as (Borucki and Summers, 1984; Sackett, 1999):

$$p \approx \frac{R_s}{a}, \quad (2.2)$$

where  $R_s$  is the radius of the star and  $a$  is the semi-major axis of the orbit.

## 2.1 Geometry of transit

Understanding of geometry of the transit light curve is important for the characterisation of the observed system. It is possible to determine a ratio of planet radius  $R_p$  and stellar radius  $R_s$  and orbital inclination  $i$  from the light curve.

There are three parameters which characterise transit. The transit depth  $\Delta F$ , the interval between the first and fourth contacts  $t_T$ , and the interval between the second and third contacts  $t_F$ , these parameters are shown in Figure 2.2 (Seager and Mallén-Ornelas, 2003). A period  $P$  can also be determined from at least two observed flux drops.

Three equations which describe the geometry of the light curve are (Seager and Mallén-Ornelas, 2003; Sackett, 1999):

$$\Delta F = \left( \frac{R_p}{R_s} \right)^2, \quad (2.3)$$

$$t_T = \frac{P}{\pi} \arcsin \left( \frac{R_s}{a} \left\{ \frac{[1 + (R_p/R_s)]^2 - [(a/R_s) \cos i]^2}{1 - \cos^2 i} \right\}^{1/2} \right), \quad (2.4)$$

$$\frac{\sin(t_F \pi / P)}{\sin(t_T \pi / P)} = \frac{\{[1 - (R_p/R_s)]^2 - [(a/R_s) \cos i]^2\}^{1/2}}{\{[1 + (R_p/R_s)]^2 - [(a/R_s) \cos i]^2\}^{1/2}}. \quad (2.5)$$

The ratio of the planet-star radius can be obtained simply from equation 2.3. Projected distance between the planet and star centres, shown in Figure 2.2 is called impact parameter  $b$  and can be calculated using equations 2.3 and 2.5 as

$$\begin{aligned} b &= \frac{a}{R_s} \cos i = \\ &= \left( \frac{(1 - \sqrt{\Delta F})^2 - [\sin^2(t_F \pi / P) / \sin^2(t_T \pi / P)](1 + \sqrt{\Delta F})^2}{1 - [\sin^2(t_F \pi / P) / \sin^2(t_T \pi / P)]} \right)^{1/2}. \end{aligned} \quad (2.6)$$

From equations 2.3, 2.4 and 2.6 we can get  $a/R_s$  ratio

$$\frac{a}{R_s} = \left( \frac{(1 + \sqrt{\Delta F})^2 - b^2[1 - \sin^2(t_T \pi / P)]}{\sin^2(t_T \pi / P)} \right)^{1/2}. \quad (2.7)$$

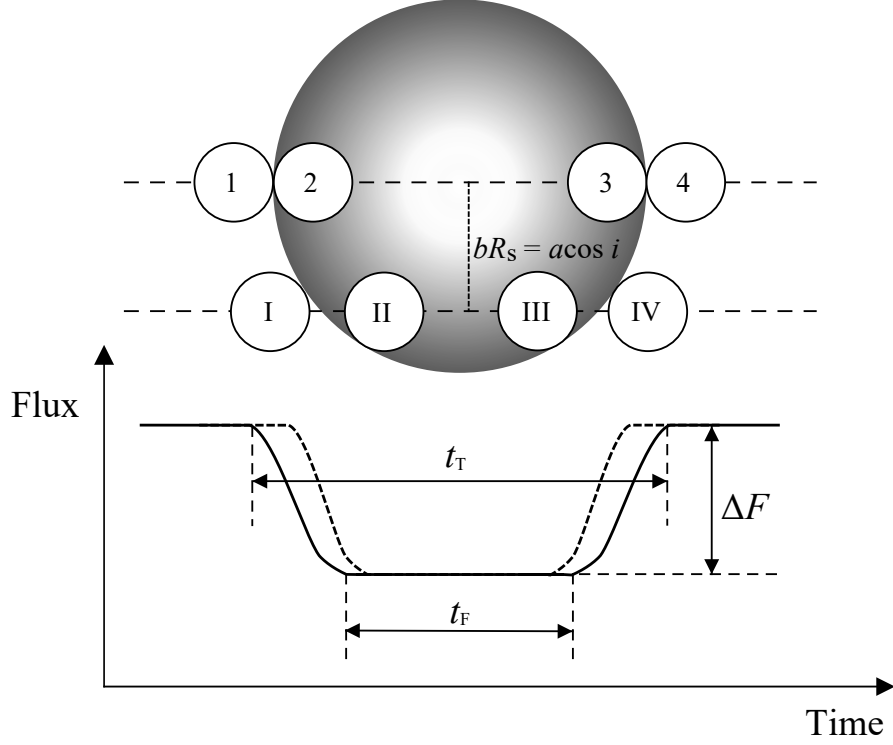


Figure 2.2: Illustration of transit. On the plot, two schematic light curves are shown, solid line belongs to the planet with arabic numerals labels and dashed line belongs to the planet with roman numerals labels. On the solid line, parameters characterising transit are marked: the transit depth  $\Delta F$ , the interval between the first and fourth contacts  $t_T$ , and the interval between the second and third contacts  $t_F$ . The meaning of the impact parameter  $b$  is also shown. Different impact parameter  $b$  (i.e., inclination  $i$ ) results in different shape of light curve.

Using equation for  $a/R_s$  (2.7) and Kepler's third law, the stellar density  $\rho_s$  can be calculated

$$\rho_s = \frac{M_s}{R_s^3} = \left( \frac{4\pi^2}{P^2 G} \right) \left( \frac{(1 + \sqrt{\Delta F})^2 - b^2 [1 - \sin^2(t_T \pi / P)]}{\sin^2(t_T \pi / P)} \right)^{3/2}. \quad (2.8)$$

The geometry of transit can be described as overlapping circles. The ratio of obscured to the unobscured flux from a uniform source is described by the expression:

$$F(p, z) = 1 - \lambda(p, z), \quad (2.9)$$

where  $p = R_p/R_s$  and  $z = d/R_s$  whereas  $d$  is the distance between the centers of the star and the planet. These parameters are shown in Figure 2.3.

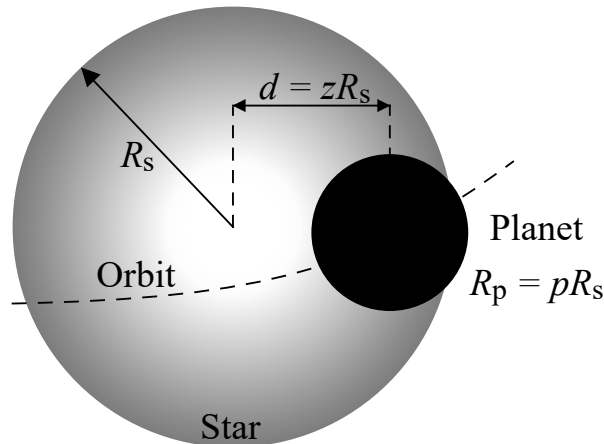


Figure 2.3: Illustration of parameters  $p$  and  $z$ . Parameter  $p$  is the planet-star radius ratio and parameter  $z$  is the ratio of the distance between the centers of the star and the planet  $d$  and the star radius  $R_s$ .

When this expression is used, there are three stages of the transit. First is when the planet is outside of the star disk which satisfies the condition  $1 + p < z$ . When the planet is outside of the star disk, so it does not occult any part of the disk then  $\lambda(p, z) = 0$ . Next part of the transit is when the star disk is occulted with the whole planet disk  $z \leq 1 - p$  and  $\lambda(p, z) = p^2$  according to equation 2.3. For partially overlapping part of the transit the expression for  $\lambda(p, z)$  is (Mandel and Agol, 2002):

$$\lambda(p, z) = \frac{1}{\pi} \left[ p^2 \kappa_0 + \kappa_1 - \sqrt{\frac{4z^2 - (1 + z^2 - p^2)^2}{4}} \right], \quad (2.10)$$

where  $\kappa_0 = \cos^{-1}[(p^2 + z^2 - 1)/2pz]$  and  $\kappa_1 = \cos^{-1}[(1 - p^2 + z^2)/2z]$ .

## 2.2 Limb-darkening

It is important to take into consideration limb darkening when generating or fitting light curves. The fact that real stars are not a uniform sources of light (e.g. see Figure 2.2) significantly change the shape of the light curve. The effect of the limb darkening is changing the light curve in three ways. It changes the transit depth  $\Delta F$ , the bottom of the light curve is rounder which is reducing  $t_F$ , and the boundary between the flat bottom and ingress/egress is less apparent as can be seen in Figure 2.4.

Limb darkening is an optical phenomenon which makes the centre of the star disk look brighter than the edge. It is caused by two reasons, the first is the direction of the radiation from the photosphere. This radiation has mainly radial direction of propagation which means that in areas farther from the center of the disk, much of the visible light already goes in a different direction than

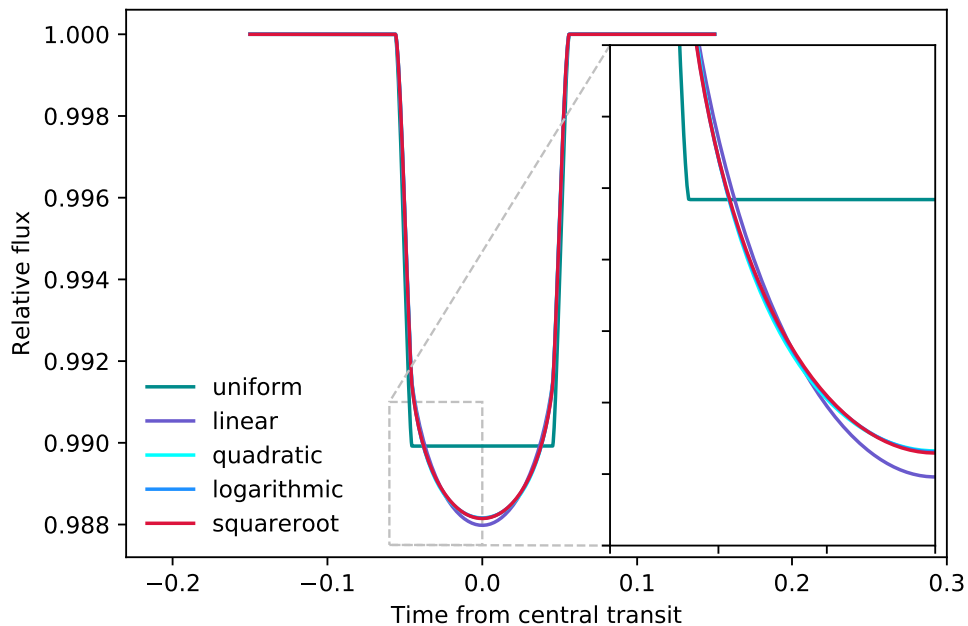


Figure 2.4: A plot showing the shape of a transit considering uniform stellar surface and using various limb-darkening laws with zoomed-in area around the light curve bottom. This plot was made using the `batman` code (Kreidberg, 2015). For the simulation, a Sun-like star and corresponding limb-darkening coefficients calculated for the TESS filter (Claret, 2017) were used.

to the observer. The second reason is the thickness of the photosphere. When the photosphere is observed from the front, we observe all its parts at once, while when observed from the side, we see separately the colder, less dense parts, which emit radiation of a different wavelength.

The first description of limb darkening considered linear darkening law (Milne, 1921). Lately, it was shown that this law is not suitable, and other models were proposed.

Linear (Milne, 1921):

$$\frac{I(\mu)}{I(1)} = 1 - u(1 - \mu), \quad (2.11)$$

Quadratic (Wade and Rucinski, 1985):

$$\frac{I(\mu)}{I(1)} = 1 - a(1 - \mu) - b(1 - \mu)^2, \quad (2.12)$$

Square root (Diaz-Cordoves and Gimenez, 1992):

$$\frac{I(\mu)}{I(1)} = 1 - c(1 - \mu) - d(1 - \sqrt{\mu}), \quad (2.13)$$

Logarithmic (Klinglesmith and Sobieski, 1970):

$$\frac{I(\mu)}{I(1)} = 1 - e(1 - \mu) - f\mu \ln(\mu), \quad (2.14)$$

Non-linear (Claret, 2000):

$$\frac{I(\mu)}{I(1)} = 1 - \sum_{n=1}^4 c_n(1 - \mu^{n/2}), \quad (2.15)$$

where  $I(1)$  is the specific intensity at the centre of the stellar disk,  $u, a, b, c, d, e, f, c_n$  are the corresponding limb darkening coefficients,  $\mu = \cos \theta = (1 - r^2)^{1/2}$ , where  $0 \leq r \leq 1$  and  $\theta$  is the angle between the normal to the star surface and the line of sight to the observer,  $\mu$  is shown in Figure 2.5.

The expression for flux with taking into consideration limb darkening is (Mandel and Agol, 2002):

$$F(p, z) = \left[ \int_0^1 I(r) 2r dr \right]^{-1} \int_0^1 dr I(r) \frac{d[F^*(\frac{p}{r}, \frac{z}{r}) r^2]}{dr}, \quad (2.16)$$

where  $I(r)$  is limb darkening law,  $F^*(p, z)$  is the flux from uniform source.

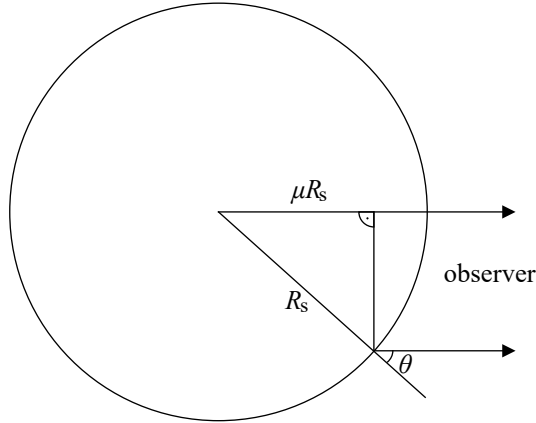


Figure 2.5: Geometry of the limb darkening.

---

## Generating the light curves

### 3.1 PyLightcurve

We used `PyLightcurve` for generating and fitting light curves of hypothetical exoplanet (Tsiaras et al., 2016). This Python package can be used for various applications for transit modelling. It can be used for the search of parameters of known exoplanets in the Open Exoplanet Catalogue database, calculation of limb darkening coefficients for different laws and filters, calculation of exoplanetary orbits, calculation of the transit model, fitting transit model and fitting real observed data.

For generating light curves we used function `plc.transit` which returns light curve according to the orbital parameters. Orbital parameters are limb darkening law, limb darkening coefficients, planet radius in units of star radii, orbital period in days, orbital semi-major axis in units of star radii, orbital eccentricity, orbital inclination in degrees, orbital argument of periastron in degrees, transit mid-time in days, length of the time sequence in days and the level of numerical precision.

Orbital parameters of our simulated exoplanet are in Table 3.1. This exoplanet is called hot Jupiter. It is a very common type of observed exoplanet because of its short orbital period (Wang et al., 2015). We used the orbital period of 2.5 days to simulate this exoplanet as easily observable from Earth i.e. with transit duration less than 12 hours and taking into account day/night cycle. Inclination  $88.7^\circ$  was used to avoid solving the ideal case of exoplanetary transit with inclination  $90^\circ$ . Eccentricity 0 and planet radius  $1 R_J$  is typical for hot Jupiters (Fabrycky and Tremaine, 2007). For a better approximation of a real observation we used random value of transit mid-time. This random value was chosen from 12 hours long time sequence of simulated observation. Semi-major axis was calculated using Kepler's third law. These parameters are very similar to some of the confirmed exoplanets e.g. WASP-65 b and K2-260 b (Gómez Maqueo Chew et al., 2013; Johnson et al., 2018).

We set our simulated star as Sun-like star. Surface gravity  $\log g = 4.5$ , effective temperature  $T_{\text{eff}} = 5800 \text{ K}$  and metallicity  $Z = 0$  (Smalley, 2005). We used square root limb darkening law with coefficients calculated for TESS (Claret, 2017). It was proposed that logarithmic and square-root limb darkening laws are

Table 3.1: Parameters of the simulated exoplanet.

|   |                       |
|---|-----------------------|
| orbital period $P$ :                                  | 2.5 days              |
| planet radius $R_p$ :                                 | 1 $R_J = 0.10040 R_s$ |
| semi-major axis $a$ :                                 | 0.036 au = 7.74 $R_s$ |
| inclination $i$ :                                     | 88.7°                 |
| eccentricity $e$ :                                    | 0                     |
| periastron $\omega$ :                                 | 90°                   |
| limb darkening coefficients<br>(square-root) $c, d$ : | 0.1012, 0.6106        |
| cadence:  | 30 min                |
|   | 2 min                 |
|   | 1 min                 |
|   | 25 sec                |
| noise $\sigma$ :                                      | 10000 ppm             |
|   | 2000 ppm              |
|   | 200 ppm               |

\* Planet radius  $R_p$  and semi-major axis  $a$  are in units of solar radii  $R_s$  ( $R_s = 696\,340$  km).

better than widely used quadratic limb darkening and linear laws for deriving parameters from transit lightcurves (Espinoza and Jordán, 2016). However these coefficients were fixed at theoretical values in our calculations and as is shown in Figure 2.4 different laws are giving very similar light curve.

For better simulation of real observed data we used cadences and noise simulating the main ground and space missions. We used 30 minutes cadence representing Kepler’s and TESS’s long-cadence setting, 2 minutes cadence represents TESS’s short-cadence setting and the most ground missions, 1 minute cadence corresponds to Kepler’s short-cadence setting and 25 seconds sampling will be used for PLATO (Ricker et al., 2015; Van Cleve and Caldwell, 2016; Schliegel, 2017; Plato, 2017). For the simulation of real data, noise with normal (Gaussian) distribution was added to the data. All observed data contain noise. Main sources of noise are photon-counting noise from the star and the background, dark current, read-out noise and additional systematics errors like random pointing variations of spacecraft. Space missions are simulated with noise with standard deviation  $\sigma = 200$  ppm<sup>1</sup> and  $\sigma = 2000$  ppm and ground-based missions with standard deviation  $\sigma = 10000$  ppm. Value 200 ppm corresponds to a star with apparent magnitude 10 mag and 2000 ppm corresponds to star with apparent magnitude 14 mag for TESS telescope 30 minutes exposure time

<sup>1</sup>ppm - one part per million, denotes one part from 1 000 000.

(Ricker et al., 2015; Schliegel, 2017). Ground-based missions are simulated with value 10000 ppm corresponding to star with apparent magnitude 11.5 mag for SuperWASP project (Smith et al., 2006).

Our choice of parameters was based on the fact that if we used shallow transit light curve with small data scattering or deep transit light curve with large data scattering it would be equivalent. Nevertheless, deep transit has the advantage that when we add large noise, the light curve can be still be identified. This fact can be seen from Figure 3.1 where examples of plotted data using function `plc.transit` are shown.

For fitting simulated data we used function `plc.TransitAndPolyFitting`. This function is using Markov chain Monte Carlo method for fitting, specifically `emcee`: The MCMC Hammer python package (Foreman-Mackey et al., 2013). This function fit data and get any of the orbital parameters. We used it for fitting planet radius, orbital semi-major axis, orbital inclination and time of the center of the transit. Other orbital parameters were fixed at the default values. Examples of output are shown in Figure 3.2 and Figure 3.3.

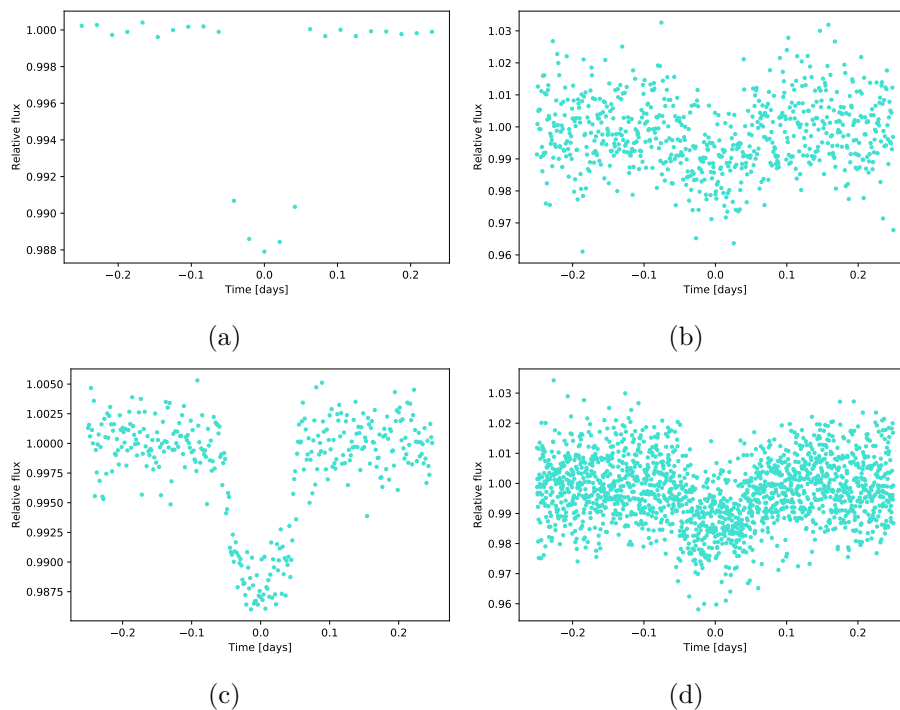


Figure 3.1: Examples of data generated with PyLightcurve with transit mid-time set to 0. In Figure (a), 30 minutes cadence with noise 200 ppm is shown. In Figure (b), 1 minute cadence with noise 10000 ppm is shown. In Figure (c), 2 minutes cadence with noise 2000 ppm is shown. In Figure (d), 25 seconds cadence with noise 10000 ppm is shown.

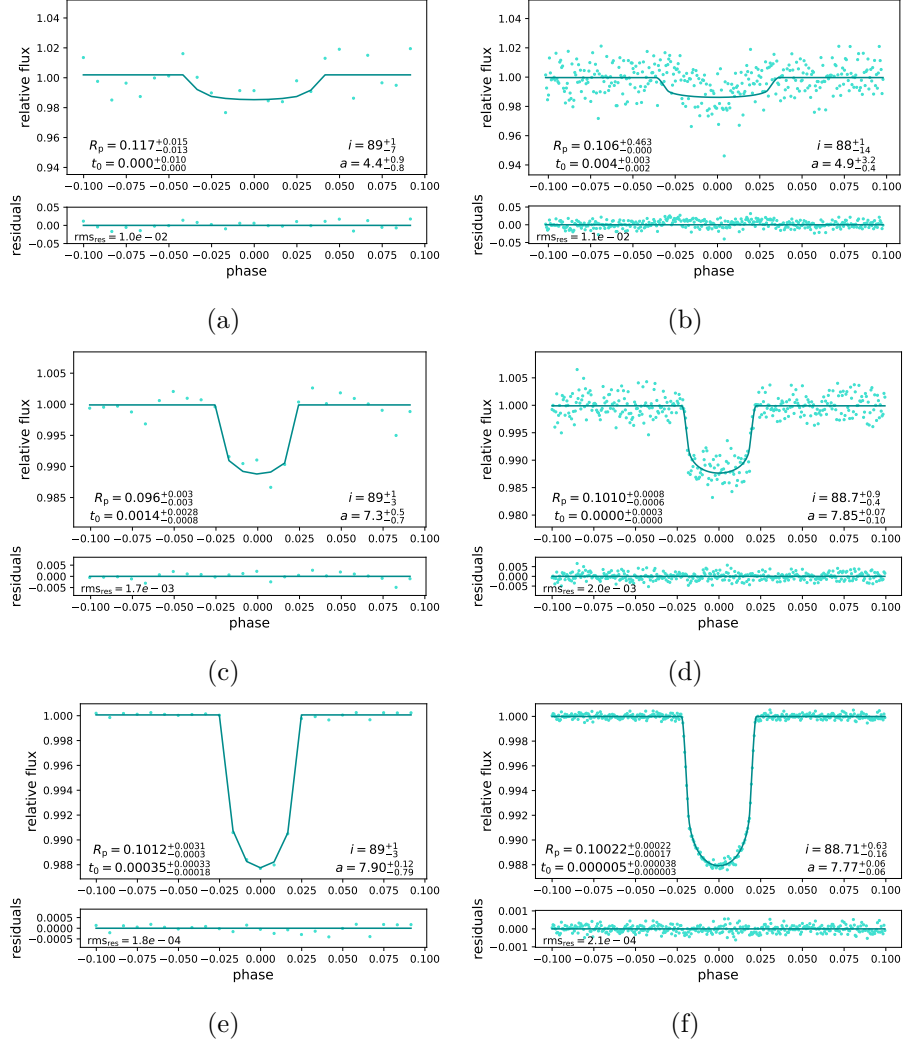


Figure 3.2: Examples of output from PyLightcurve.  $R_p$  and  $a$  are in units of solar radii  $R_s = 696\,340$  km,  $t_0$  in days and  $i$  in degrees. Transit mid-time was set to 0. Figure (a) shows simulated data with 30 minutes cadence and noise  $\sigma = 10000$  ppm. Figure (b) shows simulated data with 2 minutes cadence and noise  $\sigma = 10000$  ppm. Figure (c) shows simulated data with 30 minutes cadence and noise  $\sigma = 2000$  ppm. Figure (d) shows simulated data with 2 minutes cadence and noise  $\sigma = 2000$  ppm. Figure (e) shows simulated data with 30 minutes cadence and noise  $\sigma = 2000$  ppm. Figure (f) shows simulated data with 2 minutes cadence and noise  $\sigma = 200$  ppm.

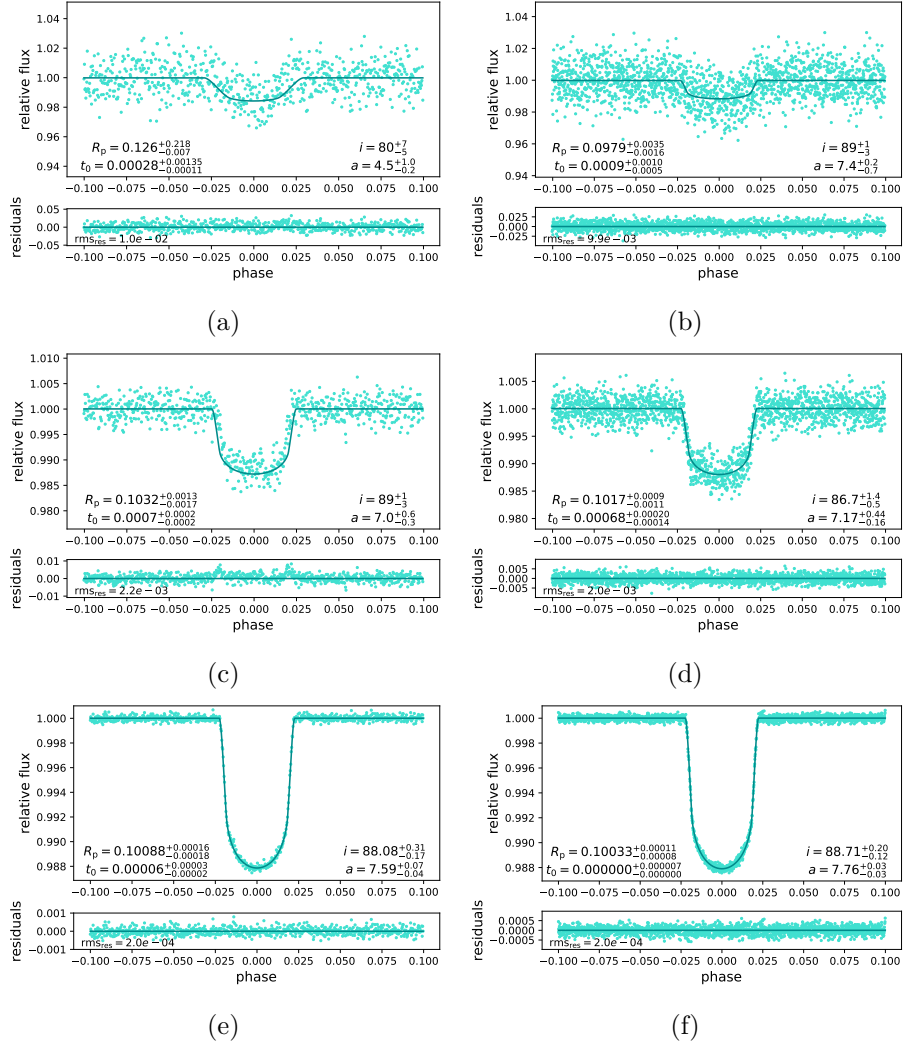


Figure 3.3: Examples of output from PyLightcurve. Units are in Figure 3.2. Transit mid-time was set to 0. Figure (a) shows simulated data with 1 minutes cadence and noise  $\sigma = 10000$  ppm. Figure (b) shows simulated data with 25 seconds cadence and noise  $\sigma = 10000$  ppm. Figure (c) shows simulated data with 1 minutes cadence and noise  $\sigma = 2000$  ppm. Figure (d) shows simulated data with 25 seconds cadence and noise  $\sigma = 2000$  ppm. Figure (e) shows simulated data with 1 minutes cadence and noise  $\sigma = 200$  ppm. Figure (f) shows simulated data with 25 seconds cadence and noise  $\sigma = 200$  ppm.

---

## Analysis of light curves

### 4.1 Light curves and fitting

Using `PyLightcurve` we made loops for 400 fitted lightcurves for 30 minutes cadence and each noise level, 200 fitted lightcurves for 2 minutes cadence and each noise, 120 fitted lightcurves for 1 minute cadence and each noise and 60 fitted lightcurves for 25 seconds cadence and each noise. A number of fitted lightcurves depends on the computing time which we set to about 10 hours. Figure 3.2 and Figure 3.3 show examples of output from `PyLightcurve` after fitting. In Figures examples of phase-folded light curves for our used cadences and data noises fitted using `PyLightcurve` are shown.

### 4.2 Results of analysis

After fitting described in section 4.1 we made averages of each fitted parameter ( $R_p, i, a$ ) for each cadence with each noise. Because transit mid-time  $t_0$  was different for each light curve we made average from the differences between the fitted value and the real randomly chosen value. These differences were also made for  $R_p, i, a$  for better illustration of the results. Standard deviations of parameters were determined. We also deleted outliers from the data by using iterative 3sigma clipping. The resulting values are listed in Table 4.1. Results for planet radius  $R_p$  are shown in Figure 4.1, 4.2, 4.3, 4.4, results for semi-major axis  $a$  are shown in Figure 4.5, 4.6, 4.7, 4.8, results for inclination  $i$  are shown in Figure 4.9, 4.10, 4.11, 4.12 and in Figure 4.13, 4.14 are shown results for transit mid-time  $t_0$ .

Table 4.1: Resulting parameter values.

| cadence      | noise [ppm] | $R_p$ [ $R_s$ ] | $a$ [ $R_s$ ] | $i$ [ $^\circ$ ] |   |
|--------------|-------------|-----------------|---------------|------------------|---|
| 30 min       | 10000       | 0.118(23)       | 7(3)          | 88.97(45)        |   |
|              | 2000        | 0.1021(48)      | 7.58(56)      | 88.80(27)        | → |
|              | 200         | 0.10027(52)     | 7.81(11)      | 88.82(15)        |   |
| 2 min        | 10000       | 0.1015(65)      | 7.62(66)      | 88.87(15)        |   |
|              | 2000        | 0.1008(16)      | 7.813(96)     | 88.74(11)        | → |
|              | 200         | 0.10036(28)     | 7.768(93)     | 88.691(36)       |   |
| 1 min        | 10000       | 0.1025(52)      | 7.73(31)      | 88.85(16)        |   |
|              | 2000        | 0.1007(11)      | 7.822(70)     | 88.74(12)        | → |
|              | 200         | 0.10035(23)     | 7.772(78)     | 88.692(40)       |   |
| 25 sec       | 10000       | 0.1022(30)      | 7.73(22)      | 88.83(16)        |   |
|              | 2000        | 0.10049(92)     | 7.825(56)     | 88.708(61)       | → |
|              | 200         | 0.10038(15)     | 7.752(50)     | 88.673(67)       |   |
| input values |             | 0.100398        | 7.745         | 88.70            |   |

|   | $\Delta t_0$ [days] | $\Delta R_p$ [ $R_s$ ] | $\Delta a$ [ $R_s$ ] | $\Delta i$ [ $^\circ$ ] |
|---|---------------------|------------------------|----------------------|-------------------------|
|   | 0.018(13)           | 0.023(18)              | 3(2)                 | 0.46(27)                |
| → | 0.0027(21)          | 0.0040(31)             | 0.43(38)             | 0.26(16)                |
|   | 0.00043(38)         | 0.00042(33)            | 0.106(78)            | 0.213(99)               |
|   | 0.0027(23)          | 0.0053(39)             | 0.51(44)             | 0.226(95)               |
| → | 0.00052(37)         | 0.0013(11)             | 0.095(70)            | 0.167(94)               |
|   | 0.000047(35)        | 0.00023(17)            | 0.077(56)            | 0.041(31)               |
|   | 0.0018(13)          | 0.0044(35)             | 0.25(19)             | 0.216(96)               |
| → | 0.00035(25)         | 0.00087(75)            | 0.087(58)            | 0.176(97)               |
|   | 0.000034(23)        | 0.00019(14)            | 0.065(51)            | 0.040(26)               |
|   | 0.00115(91)         | 0.0028(22)             | 0.17(13)             | 0.227(96)               |
| → | 0.00022(15)         | 0.00071(59)            | 0.086(48)            | 0.097(12)               |
|   | 0.000022(18)        | 0.000122(91)           | 0.039(33)            | 0.056(54)               |

### 4.2.1 Planet radius $R_p$

Results for planet radius  $R_p$  are shown in Figure 4.1, 4.2, 4.3, 4.4. We calculated relative standard deviation for better interpretation of results (see Table 4.2). In this case our expectation that with shorter cadence and decreasing noise we get better results was met. In Figure 4.2, it is shown that with 30 minutes cadence and data noise 10000 ppm the difference between fitted value and input value is  $0.02 R_s$  which means difference around 14000 km. This difference could make trouble when determining the type of exoplanet. From this analysis we can say that the data noise has a major influence on the determination of the radius.

Table 4.2: Relative standard deviations for planet radius  $R_p$

| noise<br>[ppm] | cadence    |           |          |            |
|----------------|------------|-----------|----------|------------|
|                | 30 minutes | 2 minutes | 1 minute | 25 seconds |
| 10000          | 19.5 %     | 6.4 %     | 5.1 %    | 2.9 %      |
| 2000           | 4.7 %      | 1.6 %     | 1.1 %    | 0.9 %      |
| 200            | 0.5 %      | 0.3 %     | 0.2 %    | 0.1 %      |

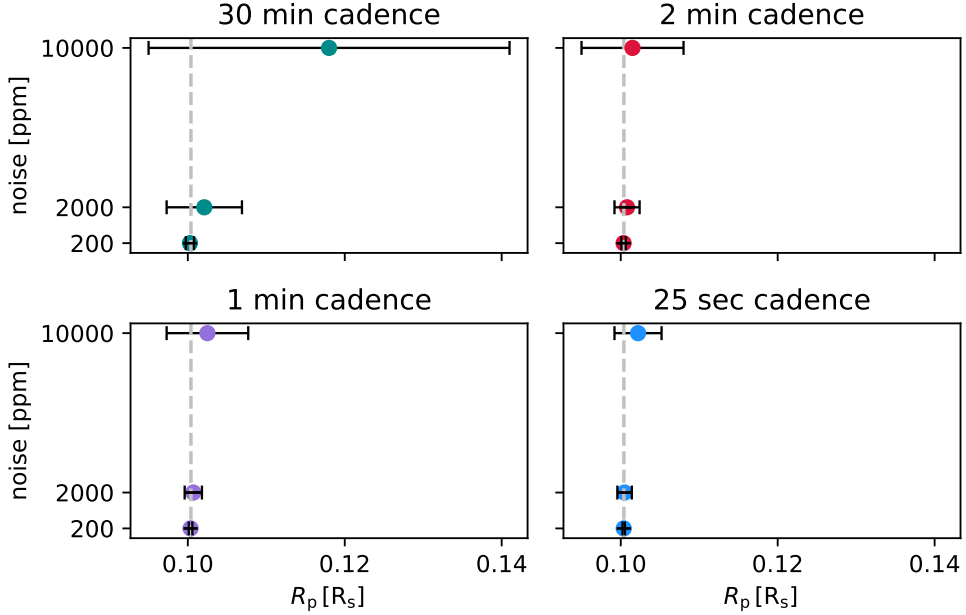


Figure 4.1: Results for the planet radius  $R_p$  depending on data noise for each cadence of data. Grey dashed line marks real value.

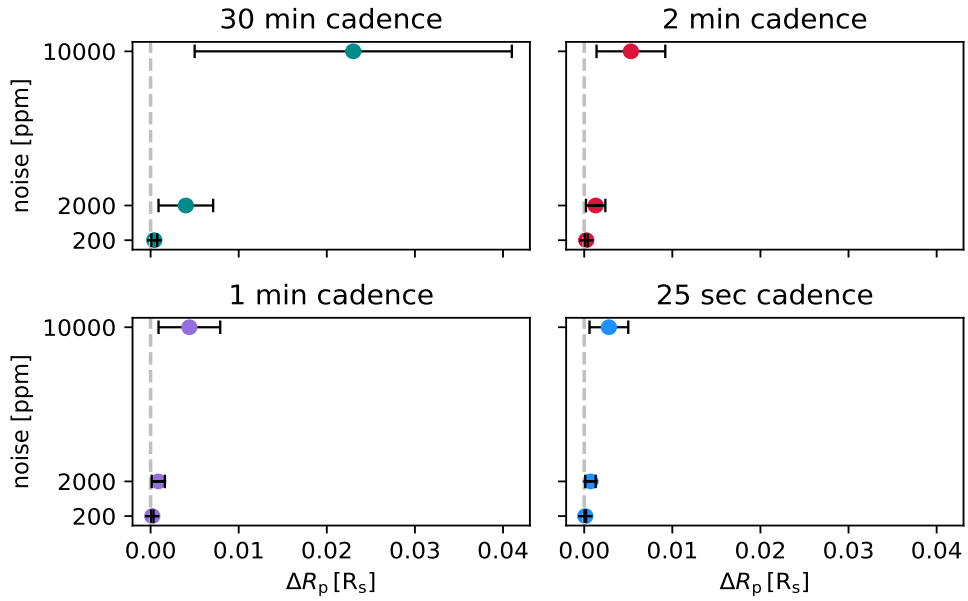


Figure 4.2: Results for the difference between real and fitted value of planet radius  $\Delta R_p$  depending on data noise for each cadence of data. Grey dashed line marks difference 0.

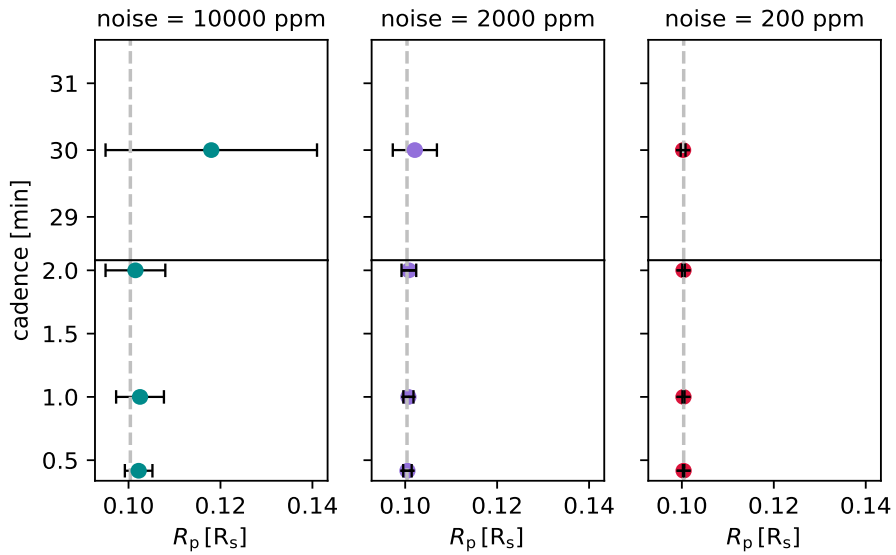


Figure 4.3: Results for the planet radius  $R_p$  depending on cadence of data for each data noise. Grey dashed line marks real value.

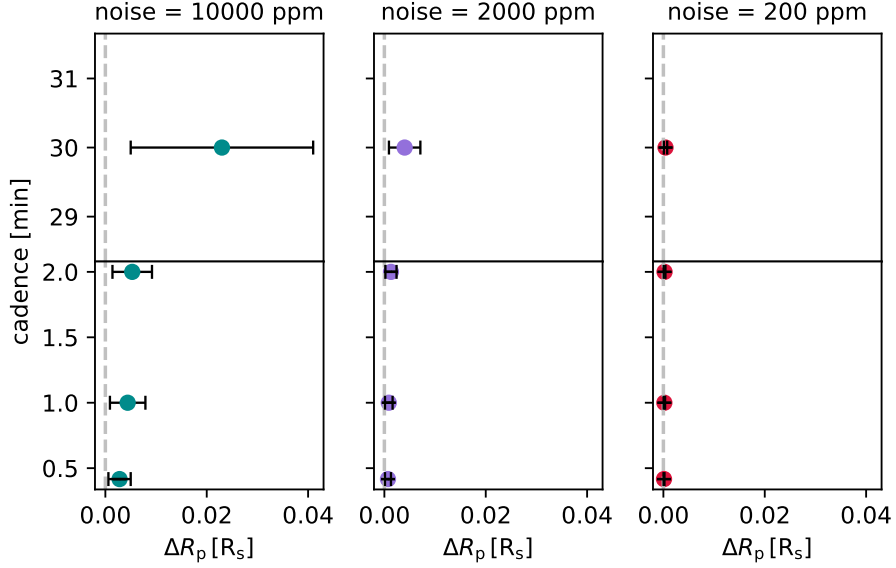


Figure 4.4: Results for the difference between real and fitted value of planet radius  $\Delta R_p$  depending on cadence of data for each data noise. Grey dashed line marks difference 0.

#### 4.2.2 Semi-major axis $a$

Results are shown in Figure 4.5, 4.6, 4.7, 4.8. Relative standard deviations are in Table 4.3. In this case our expectation that with shorter cadence and decreasing noise we get better results was also met. The worst result was again with 30 minutes cadence and data noise 10000 ppm (Figure 4.6), when the difference between input value and fitted value is approximately  $3 R_g$ . This inaccuracy could cause troubles when determining habitable zone.

Table 4.3: Relative standard deviations for inclination  $a$

| noise<br>[ppm] | cadence    |           |          |            |
|----------------|------------|-----------|----------|------------|
|                | 30 minutes | 2 minutes | 1 minute | 25 seconds |
| 10000          | 44.9 %     | 8.7 %     | 4 %      | 2.8 %      |
| 2000           | 7.4 %      | 1.2 %     | 0.9 %    | 0.7 %      |
| 200            | 1.4 %      | 1.2 %     | 1 %      | 0.6 %      |

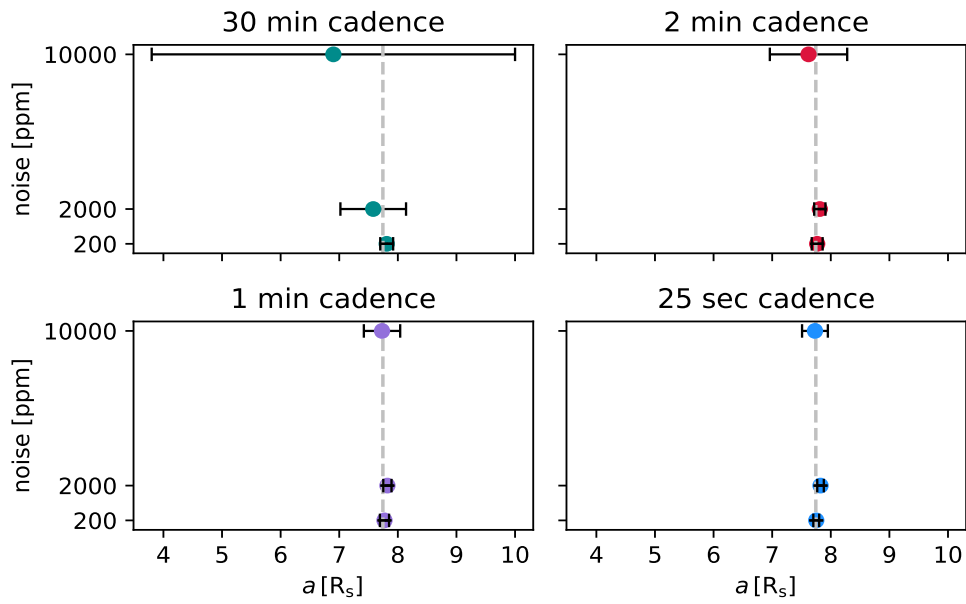


Figure 4.5: Results for the semi-major axis  $a$  depending on data noise for each cadence of data. Grey dashed line marks real value.

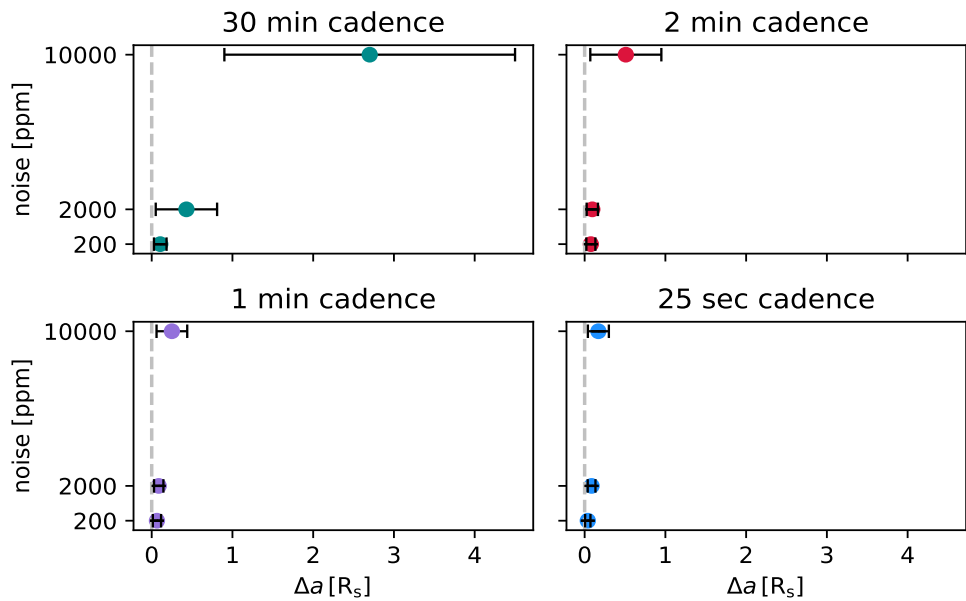


Figure 4.6: Results for the difference between real and fitted semi-major axis  $\Delta a$  depending on data noise for each cadence of data. Grey dashed line marks difference 0.

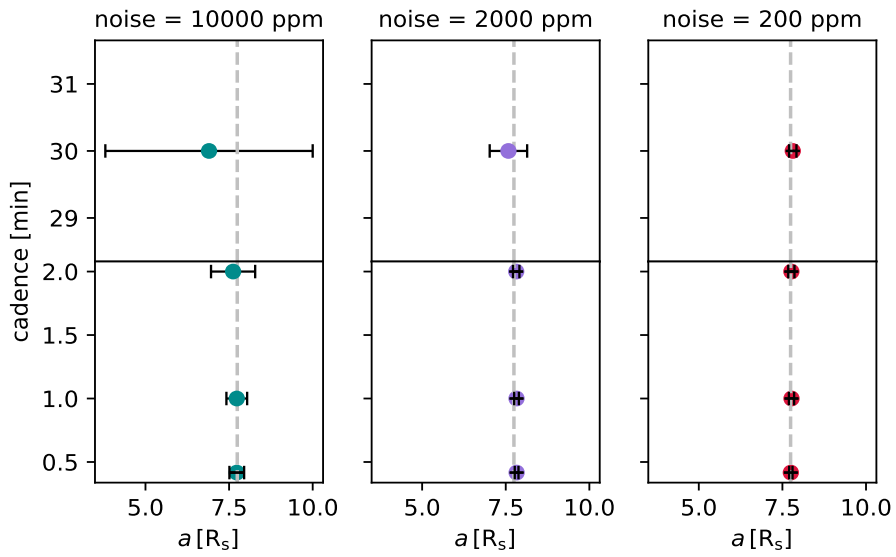


Figure 4.7: Results for the semi-major axis  $a$  depending on cadence of data for each data noise. Grey dashed line marks real value.

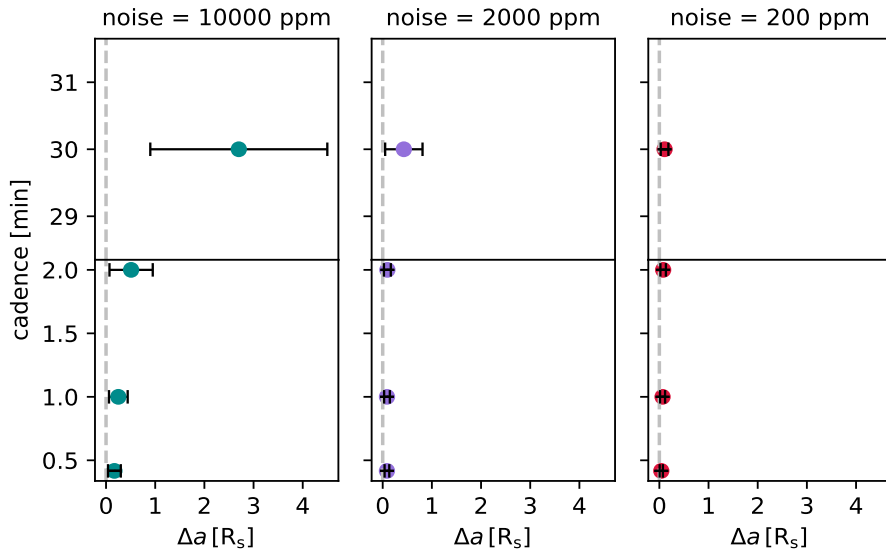


Figure 4.8: Results for the difference between real and fitted semi-major axis  $\Delta a$  depending on cadence of data for each data noise. Grey dashed line marks difference 0.

### 4.2.3 Inclination $i$

Results are shown in Figure 4.9, 4.10, 4.11, 4.12. Relative standard deviations are in Table 4.4. Determining of the inclination was successful. The biggest difference is  $0.5^\circ$ .

Table 4.4: Relative standard deviations for inclination  $i$

| noise<br>[ppm] | cadence    |           |          |            |
|----------------|------------|-----------|----------|------------|
|                | 30 minutes | 2 minutes | 1 minute | 25 seconds |
| 10000          | 0.5 %      | 0.2 %     | 0.2 %    | 0.2 %      |
| 2000           | 0.3 %      | 0.1 %     | 0.1 %    | 0.07 %     |
| 200            | 0.2 %      | 0.04 %    | 0.04 %   | 0.08 %     |

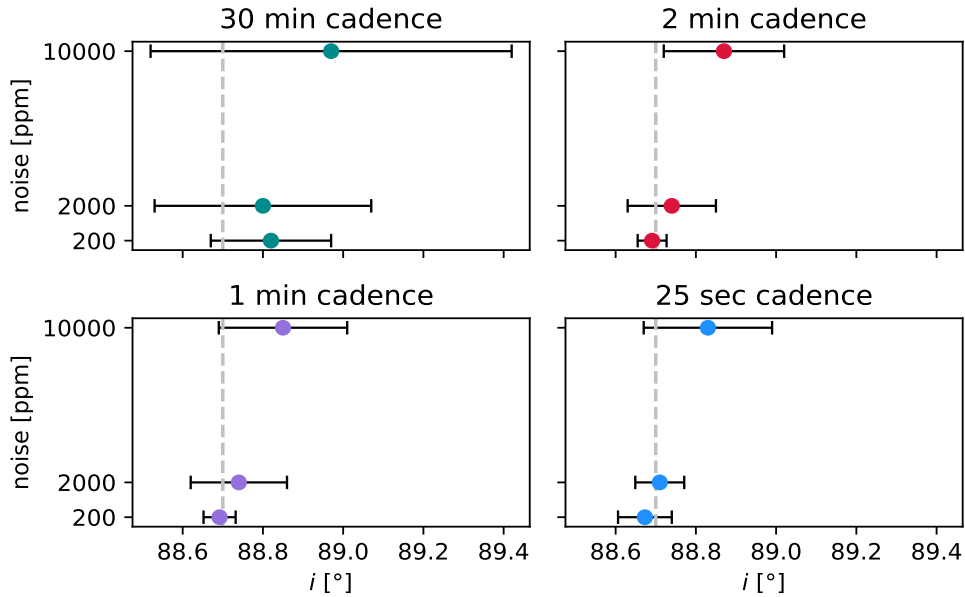


Figure 4.9: Results for the inclination  $i$  depending on data noise for each cadence of data. Grey dashed line marks real value.

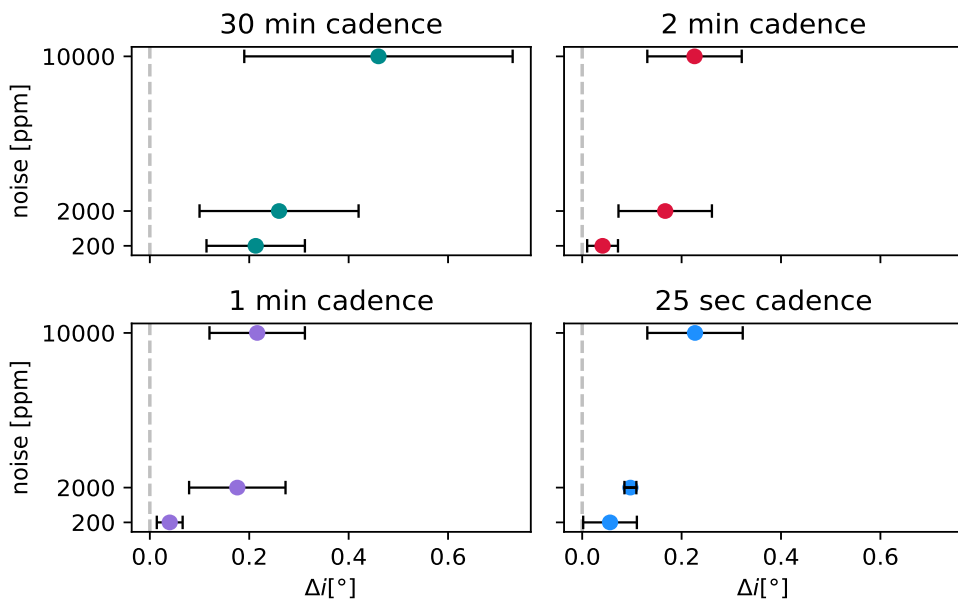


Figure 4.10: Results for the difference between real and fitted value of inclination  $\Delta i$  depending on data noise for each cadence of data. Grey dashed line marks difference 0.

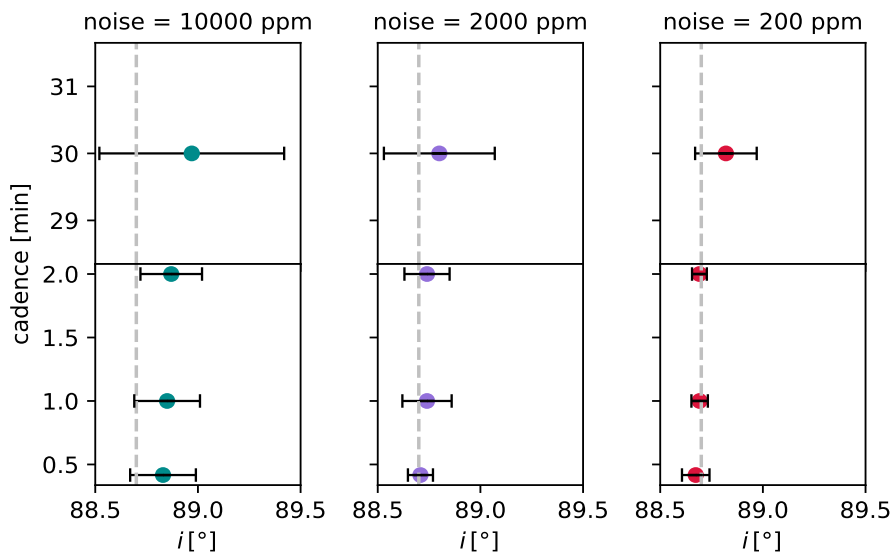


Figure 4.11: Results for the inclination  $i$  depending on cadence of data for each data noise. Grey dashed line marks real value.

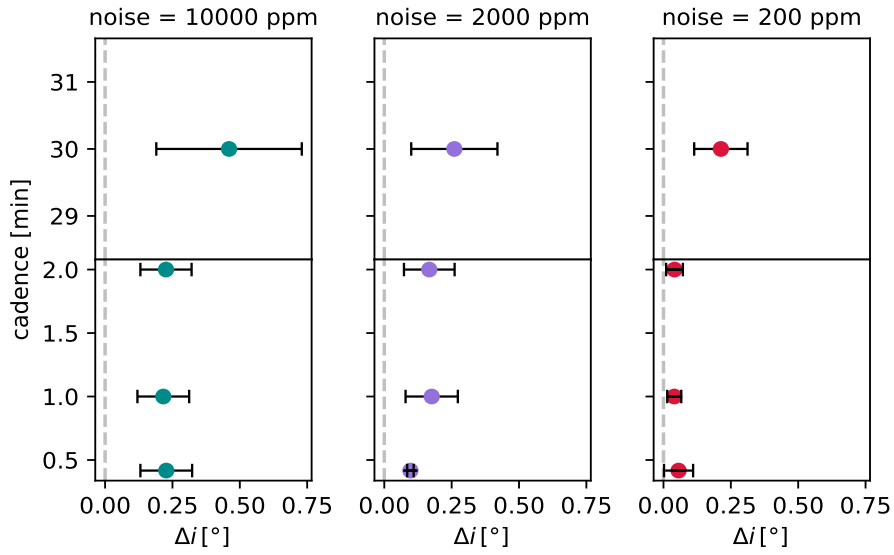


Figure 4.12: Results for the difference between real and fitted value of inclination  $\Delta i$  depending on cadence of data for each data noise. Grey dashed line marks difference 0.

#### 4.2.4 Transit mid-time $t_0$

Results are shown in Figure 4.13 and Figure 4.14. For this parameter the accuracy was really good except 30-minutes cadence with 10000 ppm. For data noise 200 ppm we can see in Figure 4.14 that the accuracy is high with any cadence. For data noise 10000 ppm and 30 minute cadence, the difference the input and the fitted value is approximately 0.02 days which is approximately 30 minutes. Planning observations with transit mid-time determined from this could be a problem.

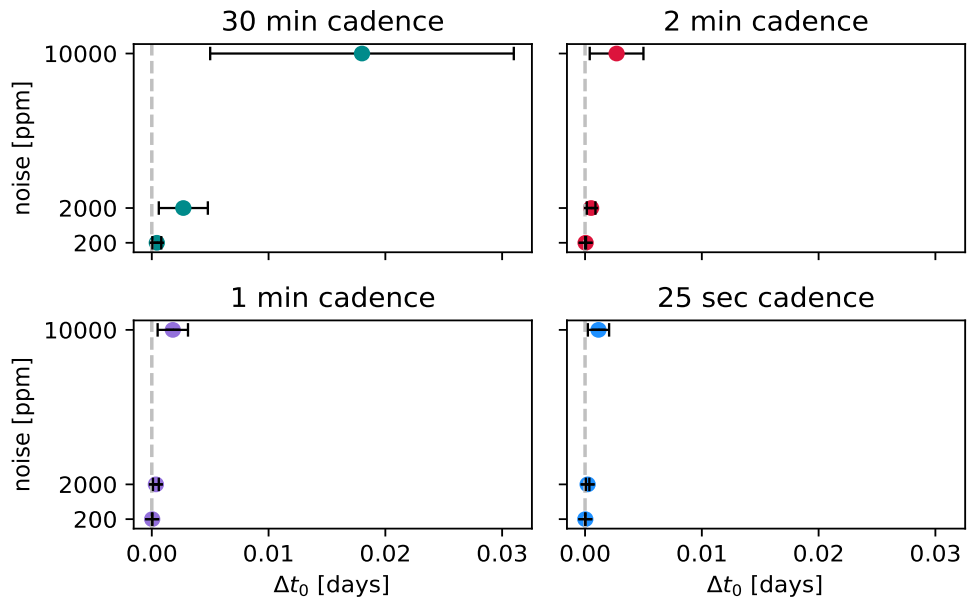


Figure 4.13: Results for the difference between real and fitted time of transit center  $\Delta t_0$  depending on data noise for each cadence of data. Grey dashed line marks difference 0.

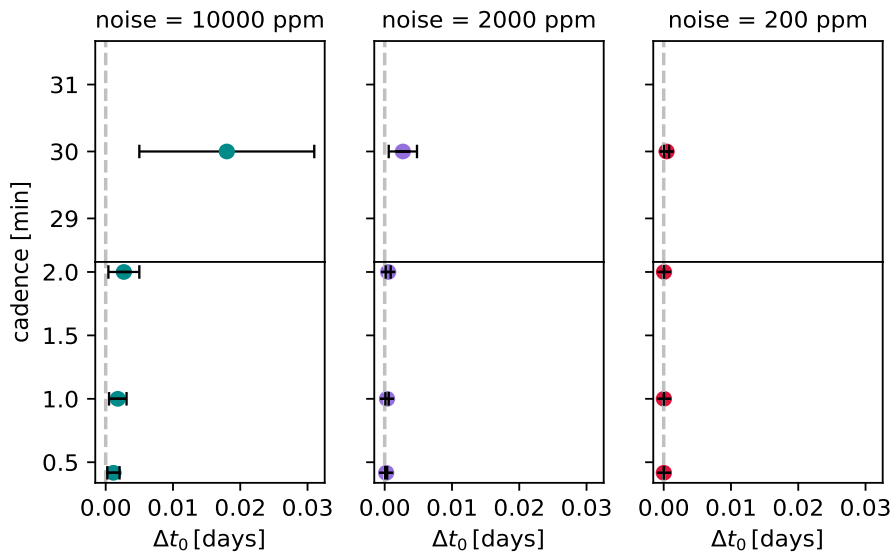


Figure 4.14: Results for the difference between real and fitted time of transit center  $\Delta t_0$  depending on cadence of data for each data noise. Grey dashed line marks difference 0.

---

## Discussion and conclusions

In this thesis, we have studied the transits of extrasolar planets, their properties and theoretical models of light curves. We used Python package `PyLightcurve` for generating 400 light curves for 30 minutes cadence (TESS, Kepler), 200 light curves for 2 minutes cadence (TESS, SuperWASP), 120 light curves for 1 minute cadence (Kepler) and 60 light curves for 25 seconds cadence (PLATO). Number of the light curves depends mainly on computing time of fitting procedure. We also added data noise so that both space and ground missions were represented. Examples of generated curves are in the Figure 3.1. To generate this data, we chose an exoplanet called hot Jupiter orbiting Sun-like star, whose parameters are in Table 3.1.

We used `PyLightcurve` for fitting generated data. It uses Markov chain Monte Carlo method for fitting, in this case python package `emcee: The MCMC Hammer`. We fitted planet radius  $R_p$ , semi-major axis  $a$ , inclination  $i$  and transit mid-time  $t_0$ . Examples of `PyLightcurve` output are shown in Figure 3.2 and Figure 3.3.

Results of the analysis are in Table 4.1. We also plotted these results for a better representation. Plots for planet radius  $R_p$  are in Figure 4.1, 4.2, 4.3, 4.4. Results for semi-major axis  $a$  are shown in Figure 4.5, 4.6, 4.7, 4.8. In Figure 4.9, 4.10, 4.11, 4.12 are shown results for inclination  $i$ . Transit mid-time  $t_0$  results are in Figure 4.13, 4.14. Relative standard deviations were calculated and for planet radius  $R_p$  are listed in Table 4.2, for semi-major axis  $a$  in Table 4.3 and for inclination  $i$  in Table 4.4.

Our expectation was that with decreasing noise and shorter cadence the accuracy would be better. This assumption was met in most cases. Biggest difference between input and fitted value was for 30 minutes cadence and data noise 10000 ppm as expected. For planet radius  $R_p$  was this difference  $0.02 R_s$  (19.5%), which is approximately 14000 km and this difference could affect the characterisation of exoplanet a lot. For semi-major axis the difference is approximately  $3 R_p$  which could mislead the determination of habitable zone. For inclination  $i$  this difference is only  $0.5^\circ$  which is quite good result. When determining transit mid-time, the difference is 0.02 days which is approximately 30 minutes. Difference in this parameter could affect planning of observations. This could be a problem for example if there was data from Kepler with this

kind of noise for 30 minutes cadence and the characterisation of exoplanet was done.

Furthermore, we can conclude that at a data noise 200 ppm, which corresponds to the observation of a star with the apparent magnitude of 10 mag and 30 minutes exposure time observed by the TESS, the determination of the parameters is comparatively accurate for all parameters. For this data noise, all parameters were determined with relative uncertainty less than 1 %.

All these results could be affected by the choice of fitting procedure. For a more accurate analysis and better understanding of this problem, it would be appropriate to generate more light curves and also try to use different routines for fitting for comparison.

## Bibliography

- [E01]. <https://exoplanets.nasa.gov>.
  - [E02]. <https://exoplanetarchive.ipac.caltech.edu>.
  - [E03]. <https://wasp-planets.net>.
  - [E04]. <https://keltsurvey.org>.
  - [E05]. <https://hatnet.org>.
  - [E06]. <https://hatsouth.org>.
  - [E07]. <https://hatsurveys.org>.
  - [E08]. <https://corot.cnes.fr/en>.
  - [E09]. <https://nasa.gov>.
  - [E10]. <https://keplerscience.arc.nasa.gov>.
  - [E11]. <https://heasarc.gsfc.nasa.gov/docs/tess>.
  - [E12]. <https://sci.esa.int/web/plato>.
  - [E13]. <https://arielmision.space>.
- Guillem Anglada-Escudé, Pedro J. Amado, John Barnes, Zaira M. Berdiñas, R. Paul Butler, and Gavin A. L. et al. Coleman. A terrestrial planet candidate in a temperate orbit around Proxima Centauri. *Nature*, 536(7617):437–440, August 2016. doi: 10.1038/nature19106.
- M. Auvergne, P. Bodin, L. Boisnard, J. T. Buey, S. Chaintreuil, and G. et al. Epstein. The CoRoT satellite in flight: description and performance. *A&A*, 506(1):411–424, October 2009. doi: 10.1051/0004-6361/200810860.
- G. Bakos, R. W. Noyes, G. Kovács, K. Z. Stanek, D. D. Sasselov, and I. Domsa. Wide-Field Millimagnitude Photometry with the HAT: A Tool for Extrasolar Planet Detection. *PASP*, 116(817):266–277, March 2004. doi: 10.1086/382735.

- G. Á. Bakos, Z. Csabry, K. Penev, D. Bayliss, A. Jordán, C. Afonso, J. D. Hartman, T. Henning, G. Kovács, R. W. Noyes, B. Béky, V. Suc, B. Csák, M. Rabus, J. Lázár, I. Papp, P. Sári, P. Conroy, G. Zhou, P. D. Sackett, B. Schmidt, L. Mancini, D. D. Sasselov, and K. Ueltzhoeffer. HATSouth: A Global Network of Fully Automated Identical Wide-Field Telescopes. *PASP*, 125(924):154, February 2013. doi: 10.1086/669529.
- Saloni Bhatiani, Xinyu Dai, and Eduardo Guerras. Confirmation of Planet-mass Objects in Extragalactic Systems. *ApJ*, 885(1):77, November 2019. doi: 10.3847/1538-4357/ab46ac.
- J. L. Birkby, R. J. de Kok, M. Brogi, H. Schwarz, and I. A. G. Snellen. Discovery of Water at High Spectral Resolution in the Atmosphere of 51 Peg b. *AJ*, 153(3):138, March 2017. doi: 10.3847/1538-3881/aa5c87.
- W. J. Borucki and A. L. Summers. The photometric method of detecting other planetary systems. *Icarus*, 58(1):121–134, April 1984. doi: 10.1016/0019-1035(84)90102-7.
- T. Castellano, J. Jenkins, D. E. Trilling, L. Doyle, and D. Koch. Detection of Planetary Transits of the Star HD 209458 in the Hipparcos Data Set. *ApJ*, 532(1):L51–L53, March 2000. doi: 10.1086/312565.
- A. Claret. A new non-linear limb-darkening law for LTE stellar atmosphere models. Calculations for  $-5.0 \leq \log[M/H] \leq +1$ ,  $2000 \text{ K} \leq T_{eff} \leq 50000 \text{ K}$  at several surface gravities. *A&A*, 363:1081–1190, November 2000.
- A. Claret. Limb and gravity-darkening coefficients for the TESS satellite at several metallicities, surface gravities, and microturbulent velocities. *A&A*, 600:A30, April 2017. doi: 10.1051/0004-6361/201629705.
- A. Collier Cameron, F. Bouchy, G. Hébrard, P. Maxted, D. Pollacco, and F. et al. Pont. WASP-1b and WASP-2b: two new transiting exoplanets detected with SuperWASP and SOPHIE. *MNRAS*, 375(3):951–957, March 2007. doi: 10.1111/j.1365-2966.2006.11350.x.
- Karen A. Collins, Keivan Stassun, B. Scott Gaudi, Thomas G. Beatty, George Zhou, David W. Latham, Allyson Bieryla, Jason D. Eastman, Robert Siverd, Justin R. Crepp, and Joshua Pepper. KELT-9b: A Case Study in Dynamical Planet Ingestion by a Hot Host Star. In *AAS/Division of Dynamical Astronomy Meeting #47*, AAS/Division of Dynamical Astronomy Meeting, page 204.03, May 2016.
- Xinyu Dai and Eduardo Guerras. Probing Extragalactic Planets Using Quasar Microlensing. *ApJ*, 853(2):L27, February 2018. doi: 10.3847/2041-8213/aaa5fb.
- J. Diaz-Cordoves and A. Gimenez. A new nonlinear approximation to the limb-darkening of hot stars. *A&A*, 259(1):227–231, June 1992.

- Néstor Espinoza and Andrés Jordán. Limb darkening and exoplanets - II. Choosing the best law for optimal retrieval of transit parameters. *MNRAS*, 457(4):3573–3581, April 2016. doi: 10.1093/mnras/stw224.
- Daniel Fabrycky and Scott Tremaine. Shrinking Binary and Planetary Orbits by Kozai Cycles with Tidal Friction. *ApJ*, 669(2):1298–1315, November 2007. doi: 10.1086/521702.
- Daniel Foreman-Mackey, David W. Hogg, Dustin Lang, and Jonathan Goodman. emcee: The MCMC Hammer. *PASP*, 125(925):306, March 2013. doi: 10.1086/670067.
- Y. Gómez Maqueo Chew, F. Faedi, D. Pollacco, D. J. A. Brown, A. P. Doyle, and A. et al. Collier Cameron. Discovery of WASP-65b and WASP-75b: Two hot Jupiters without highly inflated radii. *A&A*, 559:A36, November 2013. doi: 10.1051/0004-6361/201322314.
- James R. Graham, K. Matthews, G. Neugebauer, and B. T. Soifer. The Infrared Excess of G29–38: A Brown Dwarf or Dust? *ApJ*, 357:216, July 1990. doi: 10.1086/168907.
- Jon M. Jenkins, Joseph D. Twicken, Natalie M. Batalha, Douglas A. Caldwell, and William D. et al. Cochran. Discovery and Validation of Kepler-452b: A  $1.6 R_{\oplus}$  Super Earth Exoplanet in the Habitable Zone of a G2 Star. *AJ*, 150(2):56, August 2015. doi: 10.1088/0004-6256/150/2/56.
- M. C. Johnson, F. Dai, A. B. Justesen, D. Gandolfi, A. P. Hatzes, and G. et al. Nowak. K2-260 b: a hot Jupiter transiting an F star, and K2-261 b: a warm Saturn around a bright G star. *MNRAS*, 481(1):596–612, November 2018. doi: 10.1093/mnras/sty2238.
- D. A. Klinglesmith and S. Sobieski. Nonlinear Limb Darkening for Early-Type Stars. *AJ*, 75:175–182, March 1970. doi: 10.1086/110960.
- David G. Koch, William J. Borucki, Gibor Basri, Natalie M. Batalha, Timothy M. Brown, and Douglas et al. Caldwell. Kepler Mission Design, Realized Photometric Performance, and Early Science. *ApJ*, 713(2):L79–L86, April 2010. doi: 10.1088/2041-8205/713/2/L79.
- Laura Kreidberg. batman: BAsic Transit Model cAlculationN in Python. *PASP*, 127(957):1161, November 2015. doi: 10.1086/683602.
- A. Léger, D. Rouan, J. Schneider, P. Barge, M. Fridlund, B. Samuel, and M. et al. Ollivier. Transiting exoplanets from the CoRoT space mission. VIII. CoRoT-7b: the first super-Earth with measured radius. *A&A*, 506(1):287–302, October 2009. doi: 10.1051/0004-6361/200911933.
- Kaisey Mandel and Eric Agol. Analytic Light Curves for Planetary Transit Searches. *ApJ*, 580(2):L171–L175, December 2002. doi: 10.1086/345520.

- E. Maor. *To Infinity and Beyond: A Cultural History of the Infinite*. Chapter 24: The New Cosmology, page 198. Birkhäuser, 1987. ISBN 978-1-4612-5396-9.
- Michel Mayor and Didier Queloz. A Jupiter-mass companion to a solar-type star. *Nature*, 378(6555):355–359, November 1995. doi: 10.1038/378355a0.
- E. A. Milne. Radiative equilibrium in the outer layers of a star. *MNRAS*, 81: 361–375, March 1921. doi: 10.1093/mnras/81.5.361.
- Joshua Pepper, Richard W. Pogge, D. L. DePoy, J. L. Marshall, K. Z. Stanek, Amelia M. Stutz, Shawn Poindexter, Robert Siverd, Thomas P. O’Brien, Mark Trueblood, and Patricia Trueblood. The Kilodegree Extremely Little Telescope (KELT): A Small Robotic Telescope for Large-Area Synoptic Surveys. *PASP*, 119(858):923–935, August 2007. doi: 10.1086/521836.
- Michael Perryman. *The Exoplanet Handbook*. Cambridge University Press, 2 edition, 2018. doi: 10.1017/9781108304160.
- Plato. *Plato Definition Study Report*. 2017. URL [https://sci.esa.int/documents/33240/36096/1567260308850-PLATO\\_Definition\\_Study\\_Report\\_1\\_2.pdf](https://sci.esa.int/documents/33240/36096/1567260308850-PLATO_Definition_Study_Report_1_2.pdf). ESA-SCI(2017)1.
- D. L. Pollacco, I. Skillen, A. Collier Cameron, D. J. Christian, and C. et al. Hellier. The WASP Project and the SuperWASP Cameras. *PASP*, 118(848): 1407–1418, October 2006. doi: 10.1086/508556.
- L. Puig, G. L. Pilbratt, A. Heske, I. Escudero Sanz, and P. E. Crouzet. *ARIEL: an ESA M4 mission candidate*, volume 9904 of *Society of Photo-Optical Instrumentation Engineers (SPIE) Conference Series*, page 99041W. 2016. doi: 10.1117/12.2230964.
- George R. Ricker, Joshua N. Winn, Roland Vanderspek, David W. Latham, Gáspár Á. Bakos, and Jacob L. et al. Bean. Transiting Exoplanet Survey Satellite (TESS). *Journal of Astronomical Telescopes, Instruments, and Systems*, 1:014003, January 2015. doi: 10.1117/1.JATIS.1.1.014003.
- D. Rouan, A. Léger, J. Schneider, P. Barge, M. Fridlund, B. Samuel, D. Queloz, C. Moutou, F. Bouchy, A. Hatzes, and COROT Exoplanet Science Team. *CoRoT-7b: The First Transiting Super-Earth Fully Characterized in Radius and Mass*, volume 430 of *Astronomical Society of the Pacific Conference Series*, page 158. 2010.
- P. D. Sackett. Searching for Unseen Planets via Occultation and Microlensing. In J. M. Mariotti and D. Alloin, editors, *NATO Advanced Science Institutes (ASI) Series C*, volume 532 of *NATO Advanced Science Institutes (ASI) Series C*, page 189, January 1999.
- J. Schliegel. *TESS Observatory Guide, version 1.1*. 2017.

- S. Seager and G. Mallén-Ornelas. A Unique Solution of Planet and Star Parameters from an Extrasolar Planet Transit Light Curve. *ApJ*, 585(2):1038–1055, March 2003. doi: 10.1086/346105.
- Barry Smalley.  $T_{eff}$  and  $\log g$  determinations. *Memorie della Societa Astronomica Italiana Supplementi*, 8:130, January 2005.
- A. M. S. Smith, A. Collier Cameron, D. J. Christian, W. I. Clarkson, B. Enoch, and A. et al. Evans. The impact of correlated noise on SuperWASP detection rates for transiting extrasolar planets. *MNRAS*, 373(3):1151–1158, December 2006. doi: 10.1111/j.1365-2966.2006.11095.x.
- O. Struve. Proposal for a project of high-precision stellar radial velocity work. *The Observatory*, 72:199–200, October 1952.
- A. Tsiaras, I. P. Waldmann, M. Rocchetto, R. Varley, G. Morello, M. Damiano, and G. Tinetti. `pylightcurve`: Exoplanet lightcurve model, December 2016.
- Jeffrey E. Van Cleve and Douglas A. Caldwell. Kepler Instrument Handbook. Kepler Science Document, April 2016.
- A. van Maanen. Two Faint Stars with Large Proper Motion. *PASP*, 29(172):258, December 1917. doi: 10.1086/122654.
- R. A. Wade and S. M. Rucinski. Linear and quadratic limb-darkening coefficients for a large grid of LTE model atmospheres. *A&AS*, 60:471–484, June 1985.
- Ji Wang, Debra A. Fischer, Elliott P. Horch, and Xu Huang. On the Occurrence Rate of Hot Jupiters in Different Stellar Environments. *ApJ*, 799(2):229, February 2015. doi: 10.1088/0004-637X/799/2/229.
- A. Wolszczan and D. A. Frail. A planetary system around the millisecond pulsar PSR1257 + 12. *Nature*, 355(6356):145–147, January 1992. doi: 10.1038/355145a0.

All internet sources [E01] - [E13] were up to date on August 10, 2020.